



# Patient-derived organoids and orthotopic xenografts of primary and recurrent gliomas represent relevant patient avatars for precision oncology

Anna Golebiewska<sup>1</sup> · Ann-Christin Hau<sup>1</sup> · Anaïs Oudin<sup>1</sup> · Daniel Stieber<sup>1,2</sup> · Yahaya A. Yabo<sup>1,3</sup> · Virginie Baus<sup>1</sup> · Vanessa Barthelemy<sup>1</sup> · Eliane Klein<sup>1</sup> · Sébastien Bougnaud<sup>1</sup> · Olivier Keunen<sup>1,4</sup> · May Wantz<sup>1</sup> · Alessandro Michelucci<sup>1,5,6</sup> · Virginie Neirinckx<sup>1</sup> · Arnaud Muller<sup>4</sup> · Tony Kaoma<sup>4</sup> · Petr V. Nazarov<sup>4</sup> · Francisco Azuaje<sup>4</sup> · Alfonso De Falco<sup>2,3,7</sup> · Ben Flies<sup>2</sup> · Lorraine Richart<sup>3,7,8,9</sup> · Suresh Poovathingal<sup>6</sup> · Thais Arns<sup>6</sup> · Kamil Grzyb<sup>6</sup> · Andreas Mock<sup>10,11,12,13</sup> · Christel Herold-Mende<sup>10</sup> · Anne Steino<sup>14,15</sup> · Dennis Brown<sup>14,15</sup> · Patrick May<sup>6</sup> · Hrvoje Miletic<sup>16,17</sup> · Tathiane M. Malta<sup>18</sup> · Houtan Noushmehr<sup>18</sup> · Yong-Jun Kwon<sup>9</sup> · Winnie Jahn<sup>19,20</sup> · Barbara Klink<sup>2,9,19,20,21</sup> · Georgette Tanner<sup>22</sup> · Lucy F. Stead<sup>22</sup> · Michel Mittelbronn<sup>6,7,8,9</sup> · Alexander Skupin<sup>6</sup> · Frank Hertel<sup>6,23</sup> · Rolf Bjerkvig<sup>1,16</sup> · Simone P. Niclou<sup>1,16</sup> 

Received: 30 July 2020 / Revised: 11 September 2020 / Accepted: 12 September 2020 / Published online: 3 October 2020  
© The Author(s) 2020

## Abstract

Patient-based cancer models are essential tools for studying tumor biology and for the assessment of drug responses in a translational context. We report the establishment a large cohort of unique organoids and patient-derived orthotopic xenografts (PDOX) of various glioma subtypes, including gliomas with mutations in *IDH1*, and paired longitudinal PDOX from primary and recurrent tumors of the same patient. We show that glioma PDOXs enable long-term propagation of patient tumors and represent clinically relevant patient avatars that retain histopathological, genetic, epigenetic, and transcriptomic features of parental tumors. We find no evidence of mouse-specific clonal evolution in glioma PDOXs. Our cohort captures individual molecular genotypes for precision medicine including mutations in *IDH1*, *ATRX*, *TP53*, *MDM2/4*, amplification of *EGFR*, *PDGFRA*, *MET*, *CDK4/6*, *MDM2/4*, and deletion of *CDKN2A/B*, *PTCH*, and *PTEN*. Matched longitudinal PDOX recapitulate the limited genetic evolution of gliomas observed in patients following treatment. At the histological level, we observe increased vascularization in the rat host as compared to mice. PDOX-derived standardized glioma organoids are amenable to high-throughput drug screens that can be validated in mice. We show clinically relevant responses to temozolomide (TMZ) and to targeted treatments, such as EGFR and CDK4/6 inhibitors in (epi)genetically defined subgroups, according to *MGMT* promoter and *EGFR/CDK* status, respectively. Dianhydrogalactitol (VAL-083), a promising bifunctional alkylating agent in the current clinical trial, displayed high therapeutic efficacy, and was able to overcome TMZ resistance in glioblastoma. Our work underscores the clinical relevance of glioma organoids and PDOX models for translational research and personalized treatment studies and represents a unique publicly available resource for precision oncology.

**Keywords** Glioma · Glioblastoma · Glioma recurrence · Patient-derived orthotopic xenograft · Organoid · Preclinical models · Precision medicine · IDH1 · MGMT · VAL-083

Anna Golebiewska, Ann-Christin Hau, Anaïs Oudin equal contribution.

**Electronic supplementary material** The online version of this article (<https://doi.org/10.1007/s00401-020-02226-7>) contains supplementary material, which is available to authorized users.

✉ Simone P. Niclou  
simone.niclou@lih.lu

Extended author information available on the last page of the article

## Introduction

Candidate therapeutics for personalized treatment in rare tumors are difficult to test in clinical trials because of inter-tumor differences and the limited number of patients representing specific genetic profiles. Adult diffuse gliomas are a particularly heterogeneous group of rare brain tumors, with grade IV glioblastoma (GBM) being the most malignant subtype [67]. Despite surgery, radiotherapy and chemotherapy,

the median survival of GBM patients is 14 months, and the recurrence is inevitable. GBM, characterized as *Isocitrate dehydrogenase* wild type (IDHwt), encompasses tumors with varying genetic backgrounds that affect distinct signaling networks [11, 14]. They can be classified into molecular subtypes with differing expression signatures [107, 112], display variable DNA ploidy [92] and have different DNA methylation status of the *O*-6-methylguanine-DNA methyltransferase (*MGMT*) gene promoter. The latter has been shown to predict the response to temozolomide (TMZ) [48], the standard-of-care chemotherapeutic agent approved for GBM [94]. A separate group of adult diffuse gliomas characterized by activating *IDH1* (IDH1mut) or *IDH2* (IDH2mut) mutations comprise *1p/19q* intact astrocytomas and *1p/19q* co-deleted oligodendrogliomas, with varying grades (II–IV) and survival rates [89], further displaying, e.g., *PDGFRA* and *CDK4* amplification, *CDKN2A/B* deletion, *ATRX*, *TP53*, or *TERT* promoter mutations [60, 83, 116], as well as a glioma CpG Island Methylator Phenotype (G-CIMP) [33, 79]. Several studies point towards an evolution of diffuse gliomas upon treatment and recurrence, where IDH1/2mut astrocytomas show most and IDHwt GBMs least changes in relapsed tumors [5, 29, 38, 57]. Still, most identified changes appear idiosyncratic and it remains unclear to what extent the current standard treatment leads to molecular changes that could affect drug responses for precision medicine. So far, all targeted treatment attempts in gliomas, e.g., targeting EGFR [41], have failed in clinical trials and effective treatment strategies are urgently needed.

A major reason for the numerous failures of clinical trials is the large gap between preclinical models and the treatment situation in patients where the existing preclinical models inaccurately represent human disease. Robust brain tumor models, able to reliably predict the sensitivity of novel personalized treatments in a molecularly defined group of patients, represent an unmet need [2]. For many years, the glioma research community relied on a handful of long-term adherent GBM cell lines that undergo significant genetic drift. In vivo such cell lines do not recapitulate certain histopathological features of patient tumors and display inadequate treatment outcomes [32, 34, 103]. Some of these shortcomings can be avoided by growing cells in defined serum-free conditions as 3D tumor spheres, adapted from neural stem/progenitor cultures (generally referred to as glioma stem cell (GSC) or brain-tumor initiating cell (BTIC) cultures) [18, 62]. However, these are generally limited to classical GBM [4] and still suffer from a loss of clonal heterogeneity and molecular adaptations to culture conditions [6, 88], in particular loss of focal amplifications related to high growth factor supply in the medium [66]. Patient-derived GBM organoids derived in serum-free conditions appear as a robust in vitro alternative, with a very good preservation of a heterogeneous tissue structure [49, 51]. However, their

use is restricted by the limited availability of starting material (large amount of en bloc tissue required [51]), which is hardly compatible with modern neurosurgical practice of ultrasonic aspiration, and continuous passaging in vitro may lead to selection of proliferative GBM tumor cells. For several cancer types patient-derived xenografts (PDXs) established subcutaneously in immunodeficient animals brought a noteworthy advance, as they allow for propagation of primary patient tumors in less selective conditions and retain interactions with nonmalignant cells [16]. PDXs were shown to be more accurate in predicting treatment responses than common cell lines [46]. Several international initiatives, such as the EurOPDX and PDXNet consortia, now develop and standardize PDXs for preclinical studies [42, 72]. However, a recent evaluation of GBM PDXs highlighted drawbacks in retaining chromosomal copy number alterations (CNAs) [7], and it remains to be seen whether they represent a sustainable model for testing precision medicine regimens. As subcutaneous PDXs do not recapitulate the natural tumor microenvironment (TME), patient-derived orthotopic xenografts (PDOX) implanted directly in the brain may be more adequate for modeling gliomas in their natural milieu, preserving the physical and physiological constraints of the blood–brain barrier and the cerebrospinal fluid. To test this, it is important to assess whether PDOXs can recapitulate patient-specific genetic and epigenetic features, transcriptional programs and intratumoral heterogeneity prior and after treatment, making them amenable as patient avatars for preclinical precision medicine.

We have previously reported that short-term culture of mechanically dissociated GBM tissue fragments allows for derivation of self-organizing 3D organoids, previously referred to as organotypic spheroids, which preserve tissue structure, intercellular connections, and TME components [10, 26]. Intracranial implantation of such GBM organoids in the brain of immunodeficient rodents allowed for conservation of tumor DNA ploidy and major histopathological features, such as angiogenesis and invasiveness [12, 86, 92, 97, 111]. Such GBM PDOXs recapitulate clinical responses towards antiangiogenic agents [1, 53]. Here, we provide systematic evidence that organoid-based glioma PDOXs are reproducible and clinically relevant models for functional precision medicine. By combining tumor organoids of various glioma subtypes with *in vivo* expansion in the brain microenvironment, we present a cohort of 40 PDOX generated from primary and paired recurrent gliomas with mixed genetic backgrounds including, among others, *IDH1* mutation and distinct *EGFR* variants. We show that these PDOXs preserve key histopathological structures of malignant gliomas (grade III/IV), recapitulate tumor-intrinsic genetic and molecular features at the individual patient level and retain intratumoral transcriptomic programs and stem-cell-associated heterogeneity. This also applies to our

unique selection of matched PDOX from paired recurrent glioma samples. We further show that glioma organoids and PDOXs represent adequate patient avatars for precision oncology, also in a high-throughput manner. Drug testing in 3D organoids allows for screening *in vitro* at reasonable cost with clinically-relevant responses, which can be further validated *in vivo*. Lastly, we highlight the promising therapeutic potential of dianhydrogalactitol (VAL-083), a bifunctional alkylating agent, for treatment of GBM. In summary, our PDOX live biobank represents an important resource for accelerating the development of novel treatment strategies for glioma patients.

## Materials and methods

### Clinical samples, organoid, and PDOX derivation

Glioma samples were collected at the Centre Hospitalier of Luxembourg (CHL; Neurosurgical Department) from patients having given informed consent, and with approval from the local research ethics committee (National Committee for Ethics in Research (CNER) Luxembourg). For patient information see Supplementary Table 1, online resource. Small pieces of tissue were flash frozen for further molecular analysis. If enough tumor material was obtained, 3D organoids from patient samples were prepared as previously described [12]. Briefly, mechanically minced fresh human glioma tissue pieces, without enzymatic digestion, were seeded on agar coated flasks (0.85%) and allowed to self-organize and form organoids (previously called organotypic spheroids) for up to 2 weeks at 37°C under 5% CO<sub>2</sub> and atmospheric oxygen in DMEM medium, 10% FBS, 2 mM L-Glutamine, 0.4 mM NEAA, and 100 U/ml Pen–Strep (all from Lonza). Organoids (generation 0) with a diameter of 300–1000 µm were then implanted in the brain of immunodeficient mice (NOD/Scid or NSG; 6 organoids per mice) using a Hamilton syringe (Hamilton, Reno, NV, USA). Animals (generation 1) were maintained under SPF conditions and sacrificed at the appearance of neurological (locomotor problems, uncontrolled movements) or behavioral abnormalities (prostration, hyperactivity) and weight loss. Optionally tumor volume was monitored by MRI. Organoids (generation 1) were further prepared from minced xenografted brains in the same way as for patient tissue and serially implanted for several generations. No mechanical and enzymatic digestion was performed prior implantation. A PDOX model was considered to be established at generation 3, when tumor phenotype and animal survival appeared stable. For specific purposes, experiments were performed in nude mice and/or eGFP expressing NOD/Scid mice [78]. Samples P8, P13 and P3 were obtained from Haukeland University Hospital (Bergen, Norway) following approval

of the local ethics committee (approval number 2009/117). For these samples, organoids were initially implanted into the brain of nude rats (rnu; 10 organoids per rat: P3, P8, P13 models). Kaplan–Meier survival curves were produced in GraphPad with Wilcoxon signed-rank statistical test. The handling of animals and the surgical procedures were performed in accordance with the regulations of the European Directive on animal experimentation (2010/63/EU) and the Norwegian Animal Act, i.e., the experimental protocols were approved by the local ethics committee (Animal Welfare Structure of the Luxembourg Institute of Health; protocols LRNO-2014-01, LUPA2019/93, and LRNO-2016-01) and by the Luxembourg Ministries of Agriculture and of Health. PDOX models are available from the corresponding author or via EuroPDX consortium (<https://www.europdx.eu/>) and PDXfinder (<https://www.pdxfinder.org/>).

### Magnetic resonance imaging

During image acquisition mice were kept under anesthesia with 2.5% of isoflurane, with constant monitoring of breathing and temperature. For routine follow up, mice were placed in the MRI (3T MR Solutions) and a Fast Spin Echo T2-weighted MRI sequence was applied, with field of view of 25 mm, matrix size of 256 × 256, TE of 68 ms, TR of 3000 ms, and slice thickness of 1 mm. To visualize the contrast enhancement, T1-weighted sequences without and with contrast injection were used. Fast-Spin Echo T1-weighted MRI was defined with the following parameters: field of view of 25 mm, matrix size of 256 × 252, TE of 11 ms, TR of 1000 ms and slice thickness of 1 mm. Contrast agent (Gadodiamide, Omniscan, GE-Healthcare) at 0.5 mmol/kg was injected intravenously 1 min prior to the scan. MRI data were analyzed by ImageJ.

### Cell lines and cell line-derived xenografts

Glioma stem-like cell (GSC) cultures (P3NS, P13NS, T16NS, T158NS, T226NS, T384NS, T394NS, T407NS) were derived from PDOXs by papain-based enzymatic digestion of PDOX tissue and cultured as 3D spheres in serum-free medium based on Neurobasal® base medium (Life Technologies) supplemented with 1 × B27 (Life Technologies) 2 mM L-glutamine, 30 U/ml Pen–Strep, 1 U/ml Heparin (Sigma), 20 ng/ml bFGF (Miltenyi, 130-093-841) and 20 ng/ml EGF (Provitro, 1325950500). GSC NCH601, NCH421k, and NCH644 lines [18] were cultured as non-adherent spheres in DMEM-F12 medium (Lonza) containing 1 × BIT100 (Provitro), 2 mM L-Glutamine, 30 U/ml Pen–Strep, 1 U/ml Heparin (Sigma), 20 ng/ml bFGF (Miltenyi, 130-093-841), and 20 ng/ml EGF (Provitro, 1325950500). U87 and U251 cells (obtained from ATCC, HTB-14) were cultured as adherent monolayers in DMEM

containing 10% FBS, 2 mM L-Glutamine and 100 U/ml Pen–Strep (all from Lonza). Cell lines were regularly tested for mycoplasma contamination. Cell lines were authenticated by DNA profiling using an SNP-based multiplex approach and as compared to the other continuous cell lines in the DSMZ database. SNP profiles were unique. For in vivo experiments tumor cells (50,000–100,000 per mouse) were slowly injected through a Hamilton syringe (Hamilton, Reno, NV, USA) into the right frontal cortex. The animals were sacrificed upon weight loss, appearance of severe neurological (locomotor problems, uncontrolled movements) or behavioral abnormalities (prostration, hyperactivity).

### Immunohistochemistry and neuropathological analysis

Coronal sections from paraffin-embedded brains were stained with hematoxylin (Dako) and 1% eosin (H&E) (Sigma). For immunostaining, sections were pretreated for 5 min with Proteinase K (Dako) followed by 30 min incubation at 95 °C in retrieval solution (Dako). The Dako Envision+System-HRP was used following the manufacturer's instructions. Primary and secondary antibodies were incubated for 1 h. Signal was developed with 3,3'-diaminobenzidine chromogen in 5–20 min. Additional IHC preparations were performed using a Discovery XT automated staining module (Ventana) and standard protocols (list of antibodies in Supplementary Table 2, online resource). The existence of necrosis and the degree of invasion was assessed on the basis of H&E and human-specific Nestin staining. Proliferation index was determined as % Ki67-positive cells per whole cell population. An index of 37% was used to split Ki67 low and high models. IHC of mouse endothelial cells (CD31) was performed on isopentane flash-frozen tissues and cryostat sections (10 µm) were fixed with acetone and chloroform. Nonspecific binding was blocked with 2% FBS in TBS and antibodies were incubated for 1 h at RT. Pictures were acquired with a Leica DMI 6000B microscope. Vessel quantification was done using ImageJ software. Average vessel area (µm<sup>2</sup>) was used as a proxy for vessel abnormality. Vessel area high and low models were analyzed after median split dichotomization into two groups. Kaplan–Meier survival analyses, including Log-rank and Wilcoxon testing were performed in GraphPad Prism 8. Other analyses were performed with two-tailed Student's *t* test.

### Flow cytometry

Tumor and PDOX tissue was dissociated with MACS Neural Tissue Dissociation Kit (P) (Miltenyi) following manufacturers' instructions. For phenotyping flow experiments were performed as described [47]. Single cell suspensions were resuspended in DMEM, containing 2% FBS, 10 mM HEPES

pH 7.4, and DNase I (10 µg/ml; Sigma) at  $1 \times 10^6$  cells/ml followed by 90 min incubation with Hoechst 33342 (5 µg/ml, Bisbenzimidazole, Ho342; Sigma) at 37 °C. After washing, cells were resuspended in ice-cold HBSS 2% FBS, 10 mM HEPES pH 7.4 buffer (100 µl/test). Prior to flow cytometric analysis, cells were incubated with the IR-LIVE/DEAD® Fixable Dead Cell Stains (Invitrogen; 1 µg/ml) and appropriate pre-conjugated antibodies for 30 min at 4 °C in the dark (Supplementary Table 2, online resource). The data acquisition was performed on a FACS Aria™ SORP cytometer (BD Biosciences) fitted with a 632 nm (30 mW) red laser, a 355 (60 mW) UV laser, a 405 nm (50 mW) violet laser and a 488 nm (100 mW) blue laser was used. The data analyses were done with DIVA software (BD Bioscience). For cell sorting, single cell suspensions were stained with the TO-PRO®-3 shortly before sort. eGFP-negative tumor cells and eGFP-positive mouse non-neoplastic cells were sorted to cold flow cytometry buffer, centrifuged, and resuspended in organoid culture medium. Organoids free of non-neoplastic cells were obtained from sorted eGFP-negative tumor cells by plating 20,000 cells per well of 24-well plates precoated with agar. For mixed organoids 20,000 sorted tumor cells were premixed with 2000 sorted eGFP-positive non-neoplastic mouse cells (10%). Alternatively, FACS-sorted GFP-negative tumor cells were washed in cold HBSS buffer and processed directly to RNA extraction.

### Ploidy assessment

Nuclei were isolated from liquid nitrogen flash frozen PDOX tumors [92]. Samples were minced in DAPI buffer [10 µg/ml DAPI in 146 mM NaCl, 10 mM Tris–HCl (pH 7.5), 0.2% IPEGAL]. Nuclei were disaggregated subsequently with 20G and 25G needles and filtered through a 50 µm and a 30 µm mesh. Tumor nuclei were stained with the human-specific anti-Lamin A/C-PE antibody (Supplementary Table 2, online resource). Optionally, PDOX-derived single cell tumor cells and cell lines were stained with IR-LIVE/DEAD® Fixable Dead Cell Stains (Invitrogen; 1 µg/ml) and fixed with cold 80% ethanol. PBMCs were added to each sample as internal diploid control. Flow analysis was carried out with Aria™ SORP or Canto™ flow cytometers (BD Biosystems). DNA content was analyzed with the FlowJo software.

### Extraction and quality control of genomic DNA

DNA from flash frozen primary patient tissue, PDOX tumor tissue, PDOX-derived organoids, and GSC cultures was extracted using the AllPrep DNA/RNA Mini Kit® (Qiagen) following manufacturer's instructions for "Simultaneous purification of genomic DNA and total RNA from animal tissues". DNA was eluted in 50 µl of Nuclease-free water,

and concentrations were measured using a NanoDrop 1000 (Thermo Fisher Scientific). Integrity of gDNA was analyzed with a 1% E-Gel™ EX Agarose Gel (Thermo Fisher Scientific). To obtain DNA from formalin-fixed, paraffin-embedded (FFPE) samples, the tissue block was punched to obtain a tissue core of 2 mm containing at least 70% tumor tissue. After a deparaffinization step (Deparaffinization solution, Qiagen), DNA extraction was performed using QiAamp DNA FFPE tissue kit (Qiagen) according to the manufacturer's instruction. DNA concentrations were measured on the Qubit 4.0 fluorometer (Thermo Fisher Scientific), using the Qubit dsDNA BR Assay kit (Thermo Fisher Scientific).

### Array comparative genomic hybridization (array-CGH)

Array-CGHs were performed as previously described [92] with the following changes. DNA was fragmented (200–500 bp) using enzymatic digestion with RSA1 and Alu1 (Agilent Technologies) and labeled with the BioPrime array-CGH Genomic labeling Kit (Life Technologies) and Cy3 and Cy5 dyes (GE Healthcare) following standard protocols for Agilent array-CGH (CGH enzymatic protocol v6.2; Ref # G4410-90010). Female or Male gDNA pool (Promega) was used as a reference. All labelling reactions were assessed using a Nanodrop 1000 (Thermo Fisher Scientific) before mixing and hybridized to either a  $1 \times 1$  M,  $2 \times 400$  K,  $4 \times 180$  K or  $8 \times 60$  K SurePrint G3 human CGH microarray (Agilent Technologies) according to manufacturer's instructions (CGH enzymatic protocol v6.2; Ref # G4410-90010). Microarray slides were scanned using an Agilent 2565C DNA scanner and images were analyzed with Agilent Feature Extraction version 12.5, using default settings. The data were assessed with a series of quality control metrics and analyzed using an aberration detection (ADM2) implemented in the CytoGenomics software versions 4.2 and 5.0.2.5 (Agilent Technologies). Aberrations were called using the ADM2 algorithm with a threshold setting of 6 and an aberration filter with a minimal number of probes = 3 and a minimal AvgAbsLogRatio = 0.25. For correlation analysis, each sample was initially processed with *Agilent CytoGenomics 4.2* in order to obtain the characterization of genomics regions (BED files) described as one of the following events: “amplification”, “gain”, “loss” or “deletion. Next, from each file, only regions > 50 kb were extracted in order to construct a reference mapping file using a combination of ‘*intersectBed*’ and ‘*multiIntersectBed*’ functions from the BEDtools suite. Finally, BED files were mapped on that common reference with their corresponding type of event. As a consequence the resulting matrix represents features detectable by any of the four array types. Chromosomes X and Y were removed. Hierarchical clustering showed no bias arising from the array type used. Pearson correlation was

applied to assess relationships between genetic profiles of each sample. Next, we estimated the effects of the experimental factors on DNA copy number variation data. As these data were represented by integer values between  $-2$  and  $2$ , we were unable to fit a global linear model. Instead, we used a chi-squared contingency table test implemented in the ‘stat’ package of R. Independently for each factor and for each DNA site we tested, whether a distribution of copy numbers is different for different factor levels of the corresponding factor. Mean  $-\log_{10}(p \text{ value})$  and mean chi-squared statistics were reported for graphical presentation.

### Targeted DNA sequencing

500 ng of extracted gDNA were diluted in 130  $\mu$ l low TE buffer (Qiagen) and sheared via sonication on a Bioruptor® UCD-200 (Diagenode) to an average fragment size of 150–300 bp. DNA fragment size was determined using the DNA 1000 Kit on the Bioanalyzer 2100 (Agilent Technologies). A custom-made Agilent SureSelect<sup>XT</sup> Target Enrichment Library (Cat No. G9612B) was used for Illumina Paired-End Multiplexed Sequencing on a MiSeq® instrument (Illumina). The panel design 1 for the Target Enrichment Library was fully adapted from [85] (181 genes and 3 promoters). Further design changes were made using SureDesign—Agilent eArray (Agilent Technologies) to produce the panel design 2, containing additional regions (234 genes and 3 promoters). A total of 59 samples were sequenced 22 samples with the panel 1 and 37 samples with the panel 2. Library preparation was performed according to manufacturers' instruction. The Illumina MiSeq® Reagent Kit v3 (Cat No. MS-102-3003) was selected applying the Illumina reagent selection algorithm ([https://emea.support.illumina.com/downloads/sequencing\\_coverage\\_calculator.html](https://emea.support.illumina.com/downloads/sequencing_coverage_calculator.html)).

Variant calling was done as follows: Raw sequencing reads (fastq) were quality trimmed using the tool fastp (v. 0.20.0)[23]. Trimmed reads were aligned to an in silico fused reference genome (ICRG) containing the human genome GRCh37.75 (ENSEMBL) and the mouse genome mm10 using BWA mem (v. 0.7.17) [17]. Reads that mapped to human chromosomes were extracted from the bam file using SAMtools (v.1.9) and realigned to the human reference genome only [65]. Duplicates were annotated and removed using MarkDuplicates under GATK (v.4.0.5.1). Bam statistics were assessed using SAMtools and compared between the initial mapping to the ICRG, the realignment to the human genome and after removing duplicates. Single nucleotide variants (SNVs) and smaller insertions and/or deletions (indels) were called in the CLC Genomics Workbench (v.12.0.3) using deduplicated mappings. Variants were only called in regions with a minimum coverage of 10 reads and a minimal allele frequency of 5%. All variants that were likely to be polymorphisms and occurred in more

than 1% of the gnomAD (v.2.0.2) data base were filtered out. SNVs were annotated with COSMIC (v.89), ClinVar, and dbSNP (v.150) [61]. The primary focus in SNV calling was to determine coding changes (missense and inframe mutations), truncating (stop and frameshift mutations) and splice site mutations. Owing to poor coverage of *TERT* promoter, this region was excluded from the global analysis. All filtered variants were manually checked to exclude artefacts and variants were further classified according to the American College of Medical Genetics and Genomics (ACMG) [50]. Only pathogenic, likely pathogenic or variants of uncertain significance (VUS) were reported. For comparing the %-overlap of variants between patient tissues and PDOX, the following thresholds were applied: minimum coverage 10, minimum count 2, minimum frequency 5 %. Reads were mapped with a linear and an affine gap cost mapping and variants were merged after calling from both mappings.

Structural variants (SVs) and copy number alterations (CNAs) were analyzed using Manta (v. 1.6.0) and CNVkit (v.0.9.6) [24, 98]. For these analyzes alignment files with marked duplicates were used. SVs were annotated with SnpEff (v. 4.3.1t) [27] and filtered for variants with at least 5 supporting paired and/or split reads. CNAs were called in two separate groups, as two versions of the sequencing panels were used and the target region is important for CNA calling via CNVkit. For panel 1 no reference samples were sequenced and CNA calling was performed against a flat reference. CNAs of all samples that were sequenced with the panel 2 were normalized against a reference created from normal samples including the commercial available male (Cat No. G1471) or female (Cat No. G1521) references from Promega (Madison, Wisconsin, US) and DNA from blood of two patients. Segmentation was performed using circular binary segmentation according to default settings. Gene metrics were determined for all variants with a minimum log<sub>2</sub> deviation of 0.4. Workflow automation was performed using the workflow manager snakemake (v.5.6.0) under conda (v.4.7.12) [58]. Additional data handling was performed applying R (v.3.6) in the environment of RStudio (v.1.1.456). All CNAs and the SVs in EGFR were visualized, manually checked, and compared to available data from array-CGH and array-based DNA methylation analysis.

Subclonal deconvolution via PyClone was performed in parallel with the above data in an independent manner. PyClone input requires variants and copy number. To acquire these data, reads were aligned to hg38, processed with Picard's MarkDuplicates {<http://broadinstitute.github.io/picard/>}, and GATK indel realignment and base recalibration performed [105]. Variants were called using mpileup (Samtools v.1.9) [65] and VarScan 2's (v.2.4.4) pileup2snp and mpileup2indel commands [65] with default settings but a *p* value of 1.00. Only positions in targeted regions were kept. Variants in dbSNP were filtered out. Absolute copy

numbers were estimated using array-CGH. Log<sub>2</sub> ratios were segmented using DNACopy (v1.52.0) [87]. A custom script estimated purities and absolute copy numbers based on the assumption that chr7 likely had a clonal single copy gain, resulting in inference of one copy loss of chr10 and one copy gains of chr19 and chr20 (common events in GBM) in all analysed samples (T192, T233, T251, T158, T347, and T470), validating this approach. PyClone (v.0.13.1) [84] was run under default settings, with the addition of '-prior total\_copy\_number' to indicate the use of total copy numbers. Purities were taken from the array-CGH estimates for biopsies, and was set to 1.00 for PDOX samples.

## Digital PCR

Digital PCR was used to detect and quantify IDH1 R132H in genomic DNA using QuantStudio 3D Digital PCR System and IDH1 Digital PCR Mutation Detection Assays from Thermo Fisher (Assay ID # Hs000000036\_rm for c.395G>A (p. R132H)) according to the manufacturer's instructions. The reaction volume was 14.5 µl containing 7.5 µl QuantStudio 3D Digital PCR Master Mix v2 (Thermo Fisher Scientific, cat#: A26359), 0.73 µl of assay and sample DNA. Each assay contained forward and reverse primers, and 2 specific dye-labeled probes. The first one with a Vic reporter dye linked to the 5' end and an MGB linked to the 3' end to detect the WT allele. The second one with a FAM reporter dye at the 5' end and an MGB at the 3' end to detect the mutant allele. The thermal cycling conditions were 96 °C for 10 min; 39 cycles of 60 °C for 2 min and 98 °C for 30 s; final extension at 60 °C for 2 min. Two replicates of each sample were run and DNA input amount was 20 ng per chip. Human Genomic DNA Male (Promega, cat # G1471) and IDH1 R132H Reference Standard (Horizon, cat # HD677) were used as wild type reference DNA and positive reference respectively. Data analysis was done with the QuantStudio 3D Analysis Suite Cloud Software version 3.1.5; chips with < 15,000 partitions above the default quality threshold were omitted.

## Array-based DNA methylation Analysis

Methylation arrays with Infinium® MethylationEPIC were processed by the Helmholtz Zentrum Muenchen (Research Unit of Molecular Epidemiology/Institute of Epidemiology, German Research Center for Environmental Health, Neuberberg, Germany) [59] or by the Laboratoire National de Santé in Luxembourg. Bisulfite conversion of 250–500 ng of gDNA was done using the EZ DNA Methylation Kit (Zymo Research) according to manufacturer's procedure, with the alternative incubation conditions recommended when using the Illumina Infinium® Methylation Assay. After bisulfite treatment, Infinium HD FFPE Restore kit (Illumina)

protocol was performed on 8  $\mu$ l of DNA from FFPE samples. Genome-wide DNA methylation was assessed using the HumanMethylationEPIC BeadChip (Cat No. WG-317-1001), following the Illumina Infinium® HD Methylation protocol. This consisted of a whole genome amplification step using 4  $\mu$ l and 8  $\mu$ l (for fresh-frozen and FFPE samples, respectively) of each bisulfite converted sample, followed by enzymatic fragmentation, and hybridization of the samples to BeadChips (Illumina). After a step of single-nucleotide extension, the BeadChips were fluorescently stained and scanned with Illumina HiScan SQ scanner or iScan System. Additional Illumina HumanMethylation450 BeadChips were processed according to manufacturer's instruction at the German Cancer Research Center (DFKZ) Genomics and Proteomics Core Facility. Raw Intensity Data files (.idat) were exported from the BeadArray. Pearson correlation was applied to assess relationships between epigenetic profiles of each sample. The R package 'RnBeads' was used to generate individual 450 k and EPIC RnBeadSets [74] that were normalized using the 'BMIQ' method [100]. Both platforms were combined using the 'rnb.combine.arrays' function in order to extract only common sites present in both objects with corresponding DNA methylation level. The DNA methylation level for each locus was measured as a beta-value score; that can range from zero to one with scores of zero indicating completely unmethylated DNA and scores of one indicating complete methylated DNA. Hierarchical clustering showed no bias arising from the array type used. Pearson correlation and Principal component analysis (PCA) were applied to assess relationships between epigenetic profiles of each sample.

As several of the considered factors were strongly correlated, we estimated their importance by consequent fitting unavailable ANOVA models, independently for each CpG site and factor. Mean  $F$  statistics over all variable CpG sites was then used to illustrate the importance of the factors. To detect differentially methylated regions (DMRs) or CpGs (DMCs), IDAT files were subjected to background correction, global dye-bias normalization, calculation of DNA methylation level, and detection  $p$  values using 'methylnooob' within the 'RnBeads' package. Differential methylation analysis was conducted on genomic site and region level according to sample groups (Patient vs. PDOX or IDHwt vs. IDH1mut) using 'limma' and fitted using an empirical Bayes approach on  $M$  values [90]. In general, array probes were divided into 4 different genomic regions, giving info on functional genomic distribution: (1) tiling regions with a window size of 5kb distributed over the whole genome, (2) genes and (3) promoters annotated with Ensembl gene definitions from the biomaRt package. Promoters were defined as the region spanning 1500 bases upstream and 500 bases downstream of the TSS of the corresponding gene. (4) CpG islands tracked from UCSC genome browser. Furthermore,

probes were divided into those within CpG islands (CGI), in CGI shores, shelves, or open seas (with or without overlapping gene bodies). In the comparison between 'Patient' and 'PDOX', the following criteria were selected: adj.  $p$  value  $< 0.01$ , absolute difference in mean methylation  $\beta$  value  $> 0.2$ . Beta value distribution plots for probe categories ('Open Sea', 'Shelf', 'Shore' or 'Island') were extracted from the integrated 'Exploratory Module' from 'RnBeads'. Global beta value density plots for longitudinal samples were generated using the 'minfi' package in R, after Noob background correction and global dye-bias normalization. The analysis of CpG methylation signatures was performed as described previously [33], where DNA methylation profiles were compared to a large cohort of the patient glioma tumors. DNA methylation-based glioma classification was performed by referencing data to the dataset of over 2800 neuropathological tumors at <https://www.molecularneuropathology.org/mnp> as described previously [20].

### Genome-wide gene expression analysis

Total RNA was extracted using the QIAGEN® RNeasy Mini Kit according to the manufacturer's protocol. GeneChip® Human Gene 1.0ST Arrays were used to determine the expression profiles. Total RNAs were processed using the Ambion WT expression kit (Life Technologies) and the Affymetrix WT Terminal & Labeling kit before being hybridized on Affymetrix arrays according to the manufacturer's instructions (protocol P/N 702808 Rev.6). Upon hybridization, microarrays were washed, stained, and scanned according to manufacturer's standard procedures. Affymetrix CEL files containing hybridization raw signal intensities were processed to gene expression signals using the RMA (robust multichip average) algorithm implemented in the *oligo* package (version 1.44.0). *hugene10st-transcriptcluster.db* package version 8.7.0 was then used to map Affymetrix ID to entrez gene ID. R statistical environment was used for hierarchical clustering, principal component analysis and for empirical Bayesian statistics (LIMMA [90], R/Bioconductor). List of differentially expressed genes (DEG) were obtained with the eBayes/LIMMA. FDR was calculated with the Benjamini and Hochberg approach [8]. Thresholds were set up for FDR  $< 0.01$  and absolute fold change ( $\text{abs}(\text{FC}) \geq 2$ ). The Metascape® database [118] was used for data mining.

The similarity between our patient biopsies, PDOXs and cell lines with GBM tumors from The Cancer Genome Atlas (TCGA) cohort (538 GBM samples) was investigated using gene expression data [19]. Our cohort's data were ranked based on their interquartile ranges to select the top-5000 (most variable) probes across samples. We focused on probes with mapped gene symbols, for genes with multiple probes their expression values were (mean) merged with

Babelomics 5 [3]. Filtering resulted in 4069 unique gene symbols. TCGA data were downloaded from The Broad Institute GDAC Firehose (<http://gdac.broadinstitute.org>), and the preprocessed gene expression data (RSEM values) were analyzed. Gene symbols from our cohort were matched to the TCGA data, and 2420 unique symbols were unambiguously found in both datasets. Using the expression data for these genes, we measured (Spearman) correlation coefficients between our cohort samples and TCGA tumors. The resulting correlations with the TCGA tumors were ranked and graphically visualized in terms of individual samples and sample groups. Analyses were implemented with the R statistical language, packages *corrplot*, and *ggplot2* (<https://www.r-project.org>).

Consensus independent component analysis (ICA), a data-driven dimensionality reduction method that performs a matrix decomposition, was applied to assess signals arising from nonmalignant cells. ICA with  $k$  components represents  $\log_2$ -transformed gene expression matrix  $X$  as a matrix product of matrices  $S$  (signals) and  $M$  (weights). The first shows contribution of genes in  $k$  statistically independent signals. Biological meaning of these signals was detected by functional annotation of the most contributing genes. In order to improve reproducibility of ICA decomposition, which can be affected by the selection of initial estimations, we applied consensus ICA approach [76]. ICA was run multiple times and the resulted matrices  $S$  and  $M$  were mapped and averaged between the runs. The analysis of the cell lines and TCGA reference dataset was performed as described in [76].

### Single cell RNA-Seq using Drop-Seq

For scRNA-seq experiments PDOXs derived in nude mice were used. To obtain a pure population of single viable cells and to distinguish human tumor cells from mouse TME subpopulations PDOXs were dissociated and FACS-sorted (P3, P8, P13) or MACS-purified (T16, P13). For FACS we have separated hCD90 positive tumor cells from hCD90 negative mouse TME subpopulations [36]. MACS-based purification was performed with *Myelin Removal Beads II* followed by Mouse Cell Depletion kit (Miltenyi Biotec) according to manufacturer's protocols. Prior to cell loading on the Drop-seq chips, the viability of cells was verified and concentration was adjusted to  $\sim 150$  cells/ $\mu\text{l}$  as optimal concentration to achieve single cell encapsulation within each droplet of  $\sim 1$  nl. All samples analyzed had a cell viability  $> 95\%$ .

Microfluidics devices were fabricated using a previously published design [70]. Soft lithography was performed using SU-8 2050 photoresist (MicroChem) on 4" silicon substrate to obtain a feature aspect depth of 100  $\mu\text{m}$ . After overnight silanization (using Chlorotrimethylsilane, Sigma), the wafer masks were used for microfluidics fabrication. Drop-seq chips were fabricated using silicon based polymerization

chemistry. Briefly, Polydimethylsiloxane (PDMS) base and crosslinker (Dow Corning), were mixed at a 10:1 ratio, mixed and degassed before pouring onto the Drop-seq master template. PDMS was cured on the master template, at 80 °C for 2 h. After incubation and cooling, PDMS slabs were cut and the inlet/outlet ports were punched with 1.25 mm biopsy punchers (World Precision Instruments). The PDMS monolith was plasma-bonded to a clean microscopic glass slide using a Harrick plasma cleaner. Immediately after pairing the plasma-treated surfaces of the PDMS monolith and the glass slide, flow channels of the Drop-seq chip were subjected to a hydrophobicity treatment using 1H,1H,2H,2H-Perfluorodecyltrichlorosilane (in 2% v/v in FC-40 oil; Alfa Aesar/Sigma). After 5 min of treatment, excessive silane was blown through the inlet/outlet ports. Chips were further incubated at 80 °C for 15 min.

Experiments followed the original Drop-seq protocol [70] with minor changes. Synthesized barcoded beads (Chemgenes corp., USA) were co-encapsulated with cells inside the droplets containing lysis reagents using an optimal bead concentration of 200 beads  $\mu\text{l}^{-1}$  in Drop-seq Lysis buffer medium. Cellular mRNA was captured on the beads via barcoded oligo (dT) handles synthesized on the surface. For cell encapsulation, 2 ml of cell and bead suspensions were loaded into 3 ml syringes (BD), respectively. To keep beads in homogenous suspension a microstirrer was used (VP scientific). The QX 200 carrier oil (Bio-rad) used as continuous phase in the droplet generation was loaded into a 20 ml syringe (BD). For droplet generation, 3.6 ml per h and 13 ml per h were used in KD scientific Legato syringe pumps for the dispersed and continuous phase flows, respectively. After stabilization of droplet formation, the droplet suspension was collected into a 50 ml Falcon tube. Collection of the emulsion was carried out until 1  $\mu\text{l}$  of the single cell suspension was dispensed. Droplet consistency and stability were evaluated by bright-field microscopy using INCYTO C-Chip Disposable Hemacytometer (Fisher Scientific). Bead occupancy within droplets was carefully monitored to avoid multiple bead occupancy. The subsequent steps of droplet breakage, bead harvesting, reverse transcription, and exonuclease treatment were carried out in accordance to [70]. RT buffer contained 1 $\times$  Maxima RT buffer, 4 % Ficoll PM-400 (Sigma), 1  $\mu\text{M}$  dNTPs (ThermoScientific), 1 U/ml Rnase Inhibitor (Lucigen), 2.5  $\mu\text{M}$  Template Switch Oligo, and 10 U/ml Maxima H-RT (ThermoScientific). Post Exo-I treatment, the bead counts were estimated using INCYTO C-Chip Disposable Hemacytometer, and 10,000 beads were aliquoted in 0.2 ml Eppendorf PCR tubes. PCR mix was dispensed in a volume of 50  $\mu\text{l}$  using 1 $\times$  Hifi HotStart Readymix (Kapa Biosystems) and 0.8 mM Template-Switch-PCR primer. The thermocycling program for the PCR amplification was modified for the final PCR cycles by 95 °C (3 min), four cycles of 98 °C (20 s),



65 °C (45 s), 72 °C (3 min), 10 cycles of 98 °C (20 s), 67 °C (20 s), 72 °C (3 min) and followed by a final extension step of 72 °C for 5 min. Post PCR amplification, libraries were purified with 0.6× Agencourt AMPure XP beads (Beckman Coulter), in accordance with the manufacturer's protocol. Finally, the purified libraries were eluted in 20 µl RNase/DNAse-free molecular grade water. Quality and concentration of the sequencing libraries were assessed using BioAnalyzer High Sensitivity Chip (Agilent Technologies).

The 3' end enriched cDNA libraries were prepared by tagmentation reaction of 600 pg cDNA library using the standard Nextera XT tagmentation kit (Illumina). Reactions were performed according to the manufacturer's instructions, samples were barcoded using the N7xx index series and 400 nM custom P5 hybrid primer: (AATGATACGGCG ACCACCGAGATCTACACGCCTGTCCGCGGAAGCAGT GGTATCAACGCAGAG T\*A\*C). The PCR amplification cycling program used was: 95 °C 30 s; fourteen cycles of: 95 °C (10 s), 55 °C (30 s), 72 °C (30 s) followed by a final extension step of 72 °C (5 min). Libraries were purified twice to reduce primers and short-DNA fragments with 0.6× and 1× Agencourt AMPure XP beads (Beckman Coulter), respectively, in accordance with the manufacturer's protocol. Finally, purified libraries were eluted in 15 µl molecular grade water. Quality and quantity of the tagmented cDNA library was evaluated using BioAnalyzer High Sensitivity DNA Chip. The average size of the tagmented libraries prior to sequencing was between 400 and 700 bps. Purified Drop-seq cDNA libraries were sequenced using Illumina NextSeq 500 with the recommended sequencing protocol except for 6pM of custom primer (GCCTGTCCGCGGAAGCAGTGG TATCAACGCAGAGTAC) applied for priming of read 1. Paired end sequencing was performed with the read 1 of 20 bases (covering the random cell barcode 1–12 bases and the rest 13–20 bases of random unique molecular identifier (UMI) and for read 2 the 50 bases of the genes.

Bioinformatic processing followed the DropSeq protocol [70] using the DropSeq tool version 1.16. In brief, FASTQ files were assembled from the raw BCL files using Illumina's bcl2fastq converter and ran through the FASTQC codes [Babraham bioinformatics; <https://www.bioinformatics.babraham.ac.uk/projects/fastqc/>] to check library qualities by the assessment parameters (a) quality per base sequence, (b) per base N content, (c) per base sequence content and d) over-represented sequences. Libraries with significant deviation were re-sequenced. FASTQ files were subsequently merged and converted to binaries using PICARD's fastqtosam algorithm. The resulting digital gene expression matrix (DGE) was first cut based on knee plot analysis and subsequently filtered by the Seurat version 3 and Monocle version 2 packages (<http://cole-trapnell-lab.github.io/monocle-release/>) in R (version 3.6.0) based on ribosomal and mitochondrial

genes as well as on low transcript content. The following threshold filters were used: only cells that expressed at least 200 genes and presented  $1 \times 10^6$  total mRNAs, and only genes which were expressed in at least 5 cells were considered for further analysis. To normalize for transcript capturing between the beads, the averaged normalized expression levels ( $\log_2(\text{TPM}+1)$ ) were calculated. After filtering and normalization, our dataset included 3138 cells (per sample cell counts: P3 = 543 cells, P8 = 502 cells, P13 = 1295, T16 = 798 cells). To examine relative expression levels, we centered the data by subtracting the average expression of each gene from all cells. Digital gene expression matrix of the TME subpopulations of PDOX P8 and normal mouse brain was filtered and normalized as described above. After filtering and normalization, the dataset included 892 cells (per sample cell counts: P8 = 453 cells, Control = 439 cells). Dimensionality reduction and gene expression markers identification and visualization were done using UMAP implemented in the Seurat package version 3 [15, 93].

The cell cycle and hypoxia meta-signatures were determined based on the respective Molecular Signatures Database (MsigDB [95]) and only correlated genes ( $R > 0.3$ ) were considered. The relative expression of common signature genes between all samples was depicted in the expression heatmaps. For each cell cycle and hypoxia signature, a specific meta-module was defined, taking into account all genes that were common among the samples, and the average relative expression for each specific meta-module was calculated. These meta-modules were used to score the cells by the average relative expression of all genes in the meta-module, and cells were sorted according to these scores. The global score for each sample was calculated as the average of all cell cycle and hypoxia meta-modules expression. Meta-modules were also defined for the G1/S and G2/M phases of the cell cycle, which enabled cells to be classified as cycling (mean relative expression  $\geq 0.1$  and  $qval < 0.05$ ) and noncycling (mean relative expression  $< 0.1$  and  $qval > 0.05$ ). For each cell, the mean relative expression of unique tumor subtype genes was calculated and used to create a score for each respective subtype. The minimum and maximum score values were determined and only cell scores above the threshold ( $qval > 0.001$ ) were used to generate the tumor subtype heatmaps. Single cell signature scores for cellular phenotypic states and meta-modules (MES, AC, NPC, and OPC-like) were implemented as described by Neftel et al. [77]. TCGA subtypes of single cells were assessed based on signatures described in Wang et al. [112]. Owing to the limitations of Drop-seq data, the signature scores for TCGA subtypes were determined according to scripts from Neftel et al. [77].

## Western blot

Protein extraction was performed using minimal amounts of RIPA buffer (Thermo Fisher Scientific, Cat No. 89901) containing 1x protease inhibitor (Merck, cOmplete® protease inhibitor cocktail) and on ice incubation for 15 min followed by brief sonication and a centrifugation step (13,000 ×g, 5 min, 4 °C) to remove cellular debris. iProtein extracts were resolved in NuPage™ 4–12% BisTris Protein Gels (Cat No. NP0321BOX, Thermo Fisher Scientific, MA, US), and blotted onto an Invitrolon™ PVDF (Thermo Fisher Scientific, Cat No. LC2005) or a Nitrocellulose membrane (Lifetech, Cat No. IB23001) according to standard protocols. After incubation with 5% nonfat milk in TBST (10 mM Tris, pH 8.0, 150 mM NaCl, 0.5% Tween 20) for 60 min, the membrane was rinsed with TBST and incubated with primary antibodies (Supplementary Table 2, online resource). Membranes were washed three times for 10 min and incubated with horseradish peroxidase (HRP)-coupled secondary antibodies (Jackson ImmunoResearch) for 1 h at RT. Blots were washed with TBST three times, once with TBS, developed with a chemiluminescent substrate (ThermoFisher) and imaged with the ImageQuant 350 scanning system (cooled-CCD camera, GE Healthcare).

## Ex vivo compound screening in 384-well plate format

PDOX tumors were dissociated with the MACS Neural Dissociation kit (Miltenyi Biotec) according to manufacturer's instructions. Mouse cells were removed with Mouse Cell Depletion kit (Miltenyi Biotec). Tumor cells were seeded 1000 cells/well in organoid medium in 384-well plates (PrimeSurface®, S-Bio) and cultured for 72 h to allow organoid formation. Organoids were treated with the following compounds: Erlotinib (EGFR, SelleckChem), Gefitinib (EGFR, SelleckChem), AZD3759 (EGFR, SelleckChem), AG-490 (JAK2, EGFR, SelleckChem), Daphnetin (EGFR, PKA/C, SelleckChem), Palbociclib (CDK4/6, SelleckChem), Abemaciclib (CDK4/6, SelleckChem), TMZ (Sigma) and 1,2:5,6-Dianhydrogalactitol (VAL-083, Delmar) in a fourfold and seven-point serial dilution series ranging from 1 μM to 1 mM (VAL-083, TMZ) or 12 nM to 48 μM (remaining inhibitors). After 3 (TMZ, VAL-083) or 6 (remaining inhibitors) days of incubation at 37 °C in a 5% CO<sub>2</sub> humidified incubator for respective inhibitors, cell viability and cytotoxicity were measured with CellTiter-Glo®2.0 and CellTox™-Green assays (Promega) respectively according to the manufacturer's instructions with a ClarioStar plate reader (BMG Labtech). The relative cell viability for each dose was obtained by normalization with untreated control (VAL-083) or dimethyl sulfoxide (DMSO, Sigma, remaining

compounds) per each plate or condition. Dose response curves (DRCs) were fitted using GraphPad Prism 8: best-fit lines and the resulting IC<sub>50</sub> values were calculated using log[inhibitor] versus normalized response—variable slope (four parameters). The area under the curve (AUC) for each DRC was calculated using GraphPad Prism 8. The experiments were performed with one (VAL-083, TMZ) or two (EGFR and CDK4/6 inhibitors) biological replicates, each comprising three technical replicates per PDOX model per each drug concentration. Statistical differences between genetically defined PDOXs groups were performed with unpaired 2-tailed *t* test. For LIVE/DEAD double labeling, organoids were incubated with 2 mM Calcein-AM and 4 mM Ethidium homodimer-1 (LIVE/DEAD assay kit, Molecular Probes) for up to 6 h. Imaging of viable (green) and dead (red) cells was done using LSM510 or LSM880 Confocal Laser microscopes (Zeiss).

## Cell printing and high-throughput drug screening procedure

PDOX T434 tumors were dissociated with the MACS Neural Dissociation kit (Miltenyi Biotec) according to manufacturer's instructions. Mouse cells were removed with Mouse Cell Depletion kit (Miltenyi Biotec). Tumor cells were mixed with 1% alginate (ratio of 1:1) and printed on 384-pillar array (1000 cells with 250 nl) by ASFA Spotter ST (Medical & Bio Device, Suwon-si, South Korea). The pillars were washed by carefully combining the cell-pillar plates with 384-well plates containing 40 μl of cell culture medium (DMEM (Biowest), 10% FBS, 1% Pen–Strep, 4x NEAA (Lonza), 1% Ultraglutamine (Lonza)) in each well, and incubation for 30 min at 37 °C. The pillar plates were then combined with 384-well assay plates containing cell culture medium and incubated for 3 days at 37 °C and 5% CO<sub>2</sub> atmosphere. The pillar plates were then transferred to compound plates where the cells immobilized in alginate were exposed for 7 days to 41 FDA-approved drugs, in a fourfold and seven-point serial dilution series from 7.3 nM to 30 μM in duplicates. Bortezomib was used as an internal control. To determine end-point cell viability, the cells were stained using Calcein AM live cell staining and the images were acquired using High Content imaging instrument (CV8000, (Yokogawa, Tokyo, Japan). Cell viability was calculated based on Calcein AM fluorescence. The relative cell viability for each dose was obtained by normalization with dimethyl sulfoxide (DMSO) per each plate. The experiment was performed in two replicates on different 384 well plates. Dose Response Curves (DRC) were fitted using GraphPad Prism 8 (GraphPad). The AUC for each DRC was calculated using GraphPad Prism 8.

## In vivo tumor treatment

T16 GBM organoids were orthotopically implanted into the right frontal lobe of Swiss nude mice. Animals were monitored daily and the following criteria were evaluated: (1) loss of > 10% of body weight, (2) exhibition of strong neurological signs (3) increased kyphosis or (4) swollen belly. Tumor growth was monitored by MRI (T1- and T2-weighted MRI protocol; 3T MRI system, MR Solutions). 35 days post-implantation most mice had visible tumors and were randomized into 4 treatment groups (7 mice per treatment group, 6 mice per control group): Control, Bevacizumab (Avastin) treatment, VAL-083 treatment and combined Bevacizumab + VAL-083 treatment. Drug concentrations and treatment schedule were as follows: Bevacizumab – 20 mg/kg, 1× week, VAL-083 – 3.5 mg/kg, 3× week. Control animals received saline (NaCl 0.9%) 4× week. Compounds and saline were delivered by intraperitoneal injections. Bevacizumab and VAL-083 injections were performed on different days. 49 days after implantation MRI T2 was applied to monitor tumor progression. T1 with contrast agent was applied to several mice to evaluate the response of tumor to Bevacizumab. 56 days after implantation one mouse in control group showed neurological symptoms and was euthanized directly after MRI. T2 and T1 + contrast MRI was applied to all mice. Remaining mice were euthanized the following day before mice developed symptoms and brains extracted. Tumor volume (mm<sup>3</sup>) was measured in ImageJ as the sum of area obtained by tumor delineation in each slice and multiplying by slice thickness (1mm). Growth rate (GR) was calculated using the TV measurement as  $GR = 100 \times \log(TV_f/TV_0)/(t_f - t_0)$ , where TV<sub>f</sub> and TV<sub>0</sub> are the tumor volumes at the late (day 56) and early (day 35 or day 49) time points, respectively, and t<sub>f</sub>–t<sub>0</sub> is the difference in days between the time points. Tumor volumes are expressed in mm<sup>3</sup> and GR in % per day [80]. Statistical difference was assessed with ANOVA with Turkey's multiple comparison test.

## Statistical tests

Different statistical approaches have been applied based on the data type and measurements across the manuscript. Statistical tests are described in each paragraph above corresponding to the associated experimental procedures. If not specified above, significant differences were calculated with the Student's *t* test.

## Data availability

Our PDOX models are freely available to the scientific community. To facilitate the access to established models, we provide detailed information for the best characterized

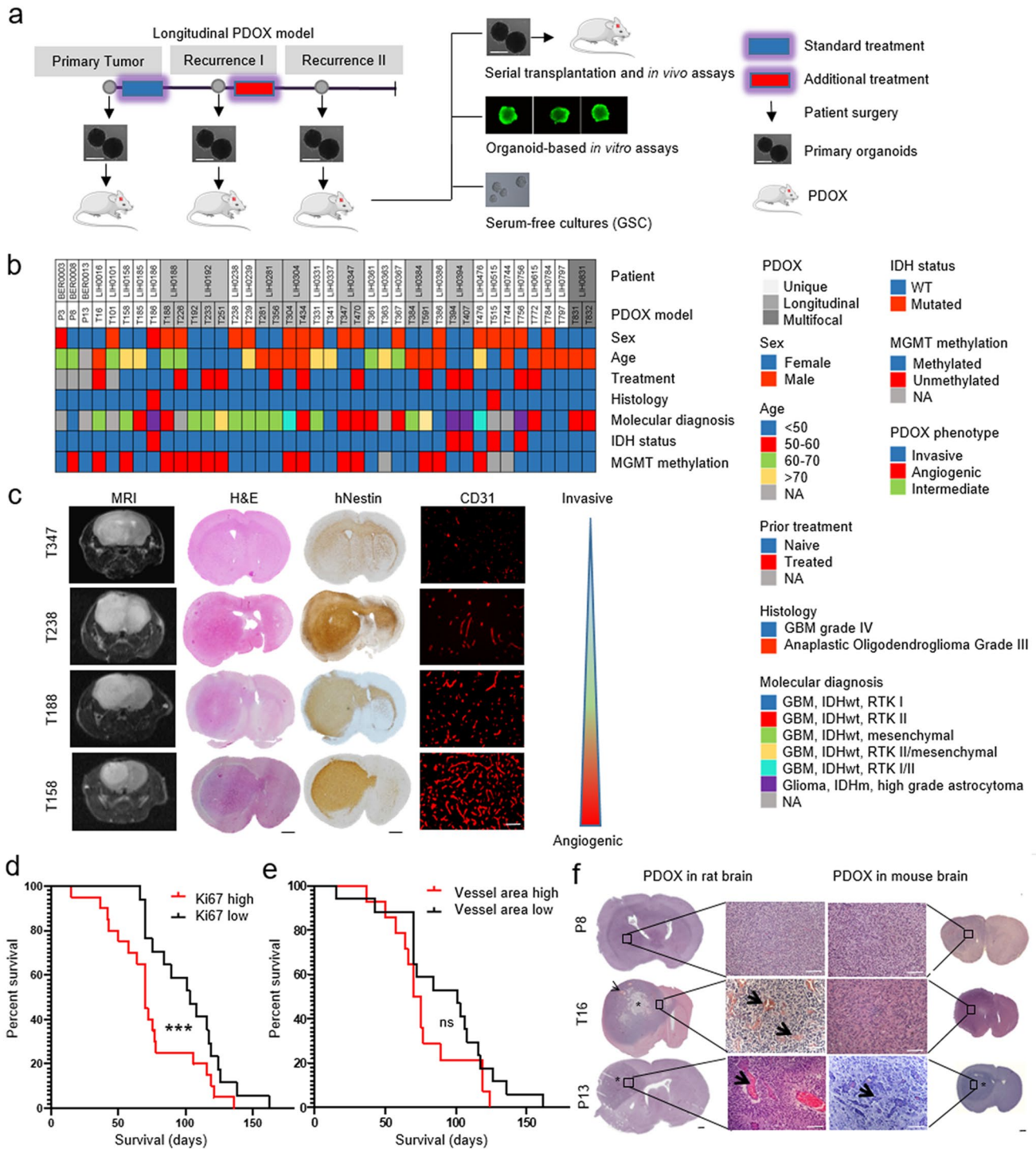
models via PDXFinder (<https://www.pdxfinder.org/>) [30]. New models will be regularly added to the resource with molecular and histopathological characterization. Our collection is also part of the EuroPDX consortium (<https://www.europdx.eu/>). Models are available from the corresponding author on reasonable request. The sharing procedure will depend on the expertise of the requesting laboratory. Groups experienced in organoid culture and intracranial implantation will be provided with the organoids. For less experienced groups we provide additional training or perform collaborative experiments in house. For small scale experiments we provide ready-to-use material, e.g., tissue sections, cryopreserved organoids, or single cells.'

Molecular data are available in the Gene Expression Omnibus repository (<https://www.ncbi.nlm.nih.gov/geo/>) under accession numbers as follows: (1) array-CGH: GSE137959; (2) DNA methylation: GSE137845; (3) gene expression: GSE134470; (4) scRNA-seq: GSE128195. Targeted DNA sequencing is available in the Sequence Read Archive (<https://www.ncbi.nlm.nih.gov/sra/>) under accession number PRJNA627814.

## Results

### Glioma organoids and PDOXs can be generated across diverse clinical high-grade glioma specimens

Fresh tumor samples of 241 glioma patients (189 GBM, 52 grades II–III gliomas) were collected at surgery, including from multifocal samples and longitudinal samples of patients undergoing sequential operations (Fig. 1a, b, Supplementary Table 1, online resource). Organoids of 300–1000 μm were obtained by mechanical dissociation of tissue, without enzymatic digestion, followed by self-aggregation in short-term culture (up to 14 days). These cultures represent self-organizing structures, which preserve a heterogeneous 3D tumor tissue organization, including cell–cell interactions, non-neoplastic cells of the tumor microenvironment (TME) and extracellular matrix components. The initial culture step allows to shed necrotic cells and to standardize the organoids for intracranial implantations. Sufficient material was available for cultures from 72% (136 GBM, 37 grades II–III gliomas, total 173) of collected patient samples, of which 79% GBMs (107/136) and 68% (25/37) of grades II–III gliomas presented high quality organoids. Common reasons for lack of healthy organoids were necrotic tissue, tissue damage during surgical procedure or insufficient material. In general, organoids self-assembled into 3D structures within 3–5 days. The proliferation and growth of organoids was generally limited, but variable and patient specific. We used patient-derived organoids for downstream applications within 10–14 days of short-term



culture. Occasionally we mechanically recut larger organoids to ensure good quality and avoid necrosis. Although organoids can remain viable in culture over longer periods, they often fuse to re-aggregate into larger structures. We have not attempted further expansion and passaging in order to limit in vitro selection processes. Organoids were either frozen in DMSO-containing medium for later recovery or directly implanted into the rodent brain. No enzymatic or mechanical

dissociation of organoids was applied prior implantation or cryopreservation.

To date, out of the 173 generated glioma organoids, we have performed 49 implantations into the mouse brain (41 GBM and 8 grade III gliomas). Organoids were implanted in immunodeficient mice (NOD/Scid, NSG) and tumors developed within 4–57 weeks depending on the parental tumor (Generation 1). The developed tumors were further

**Fig. 1** Clinical and histological characterization of the glioma PDOX cohort. **a** Schematic of derivation of PDOXs from primary and recurrent patient gliomas. Treatment refers to patients. PDOXs enable tumor expansion via serial transplantation, organoid-based in vitro assays including drug screening, genetic manipulations, and derivation of long-term in vitro sphere cultures. **b** Clinical patient information of corresponding 40 PDOXs (from 32 patients). PDOXs derived from longitudinal or multifocal samples of the same patients are highlighted. See Supplementary Table 1, online resource for more information. **c** MRI, Hematoxylin/Eosin, human-specific Nestin, and mouse-specific CD31 stainings were performed to assess histopathological characteristics of PDOXs. Representative PDOX models displaying a range of invasive and angiogenic features are shown. Scale bars represent 1mm (black) and 100µm (white). **d** Kaplan–Meier survival curves of PDOXs divided in high and low Ki67 positive cells (mean Ki67 positive cells per model - split by median), \*\*\* $p_{\text{value}} < 0.001$  (Wilcoxon signed-rank test). Mean survival of each model  $\geq$  generation 3 was plotted in each group. **e** Kaplan–Meier survival curves of PDOXs divided by vessel area (Average vessel area in µm—split by median value), ns = not significant (Wilcoxon signed-rank test). Mean survival of each model  $\geq$  generation 3 was plotted in each group. **f** Histopathological comparison of the same PDOXs derived in mice or rats. Angiogenic features are amplified in the rat brain (arrows, abnormal vessel morphology; stars, pseudopalisading necrosis; black bar, 1 mm; white bar, 100 µm). Examples are shown for pronounced invasive histopathology (P8), intermediate (T16) and increased angiogenic (P13) growth. Scale bars represent 1 mm. See more examples in Supplementary Fig. 1d, online resource

resected from the mouse brain and organoids (Generation 1) were obtained by applying the same protocol as for patient tumor tissue. IDHwt GBM organoids survived well a freezing–defrosting procedure, while IDH1mut (*R132H*) gliomas were more fragile, often requiring implantation of freshly prepared organoids or small unprocessed tissue fragments. Generally, mice showed a longer latency period at first passage (Supplementary Fig. 1a, online resource) and the most PDOXs reached a stable tumor development time per patient tumor at Generation 2–4. Successful engraftment and PDOX propagation via serial transplantation (> 3 passages) were obtained for 86% of GBMs (35/41, 6 failed due to poor organoid quality), 25% of grade III gliomas (2/8, no association with organoid quality). Grade II gliomas were not systematically implanted because of minimal prior success. Rare activating IDH2mut (*R172K*) gliomas are not yet present in the cohort. Three additional GBMs (PDOXs P3, P8, and P13) were initially derived in nude rats [111] and were further serially transplanted in mice. To date, we have generated a cohort of 40 glioma PDOX models from 32 patients, displaying different clinical characteristics and molecular backgrounds (Fig. 1b, Supplementary Table 1, online resource). Our PDOX cohort contains tumors from primary untreated gliomas as well as recurrent tumors after treatment. We obtained paired longitudinal samples, before and after treatment, from 7 patients and were able to generate 15 corresponding PDOXs. One patient (LIH0831) with a multifocal GBM led to 2 PDOX models derived

from tumor tissue collected from two distinct locations. Out of 25 PDOX models cultured in serum free medium in vitro, 8 glioma stem cell-like (GSC) lines could be propagated long term, including 2 cell lines carrying the IDH mutation (Supplementary Table 1, online resource).

### Glioma PDOXs display a range of invasive and angiogenic glioma features

PDOXs derived in immunodeficient mice preserved the major histopathological features of patient tumors and displayed a gradient of invasiveness and vascular pathology depending on the tumor of origin (Fig. 1c). Angiogenic tumors tended to grow in a more circumscribed manner and showed contrast enhancement on MRI, indicative of blood brain barrier disruption. In line with our previous report [12], mouse survival was a result of a combination of histopathological features (vascular proliferation, necrosis, and invasion) and proliferation index, where high proliferation correlated significantly with poor prognosis (Fig. 1d, e, Supplementary Table 1, online resource). Models derived from relapsed GBMs showed similar survival and proliferation index as compared to treatment-naïve tumors (Supplementary Fig. 1b, c, online resource). Based on the previous experiments with GBM PDOXs generated in rats [111], we were surprised to find that only a few PDOX models in mice displayed extensive abnormalities in blood vessels. Therefore, we compared identical patient GBMs implanted in either mouse or rat brain. While invasive tumors were similar in mice and in rats, vessel abnormalities were exacerbated in rats in the PDOXs showing only moderate defects in the mouse brain (Fig. 1f, Supplementary Fig. 1d, online resource), including pseudopalisading necrosis, dilated vessels, and endothelial cell proliferation. This indicates that the capacity of human GBM to induce angiogenesis is higher in rats as compared to mice, likely due to differences in size and cross-species interactions. These interspecies differences were also observed in xenografts derived from serum-free GSC lines (Supplementary Fig. 1d, online resource).

### Tumor development was independent of non-neoplastic cells present in organoids

Non-neoplastic cells of the TME constituted between 3 and 25% of all cells in tumor cores in different PDOX models (Supplementary Fig. 1e, online resource) and these proportions remained stable over serial transplantations. To assess whether the nontumor compartment present within organoids influenced tumor formation upon implantation in vivo, we derived TME-free organoids from FACS-purified tumor cells grown in eGFP-expressing mice and compared them with TME-containing organoids (Supplementary Fig. 1f–g, online resource). Both conditions allowed for reformation

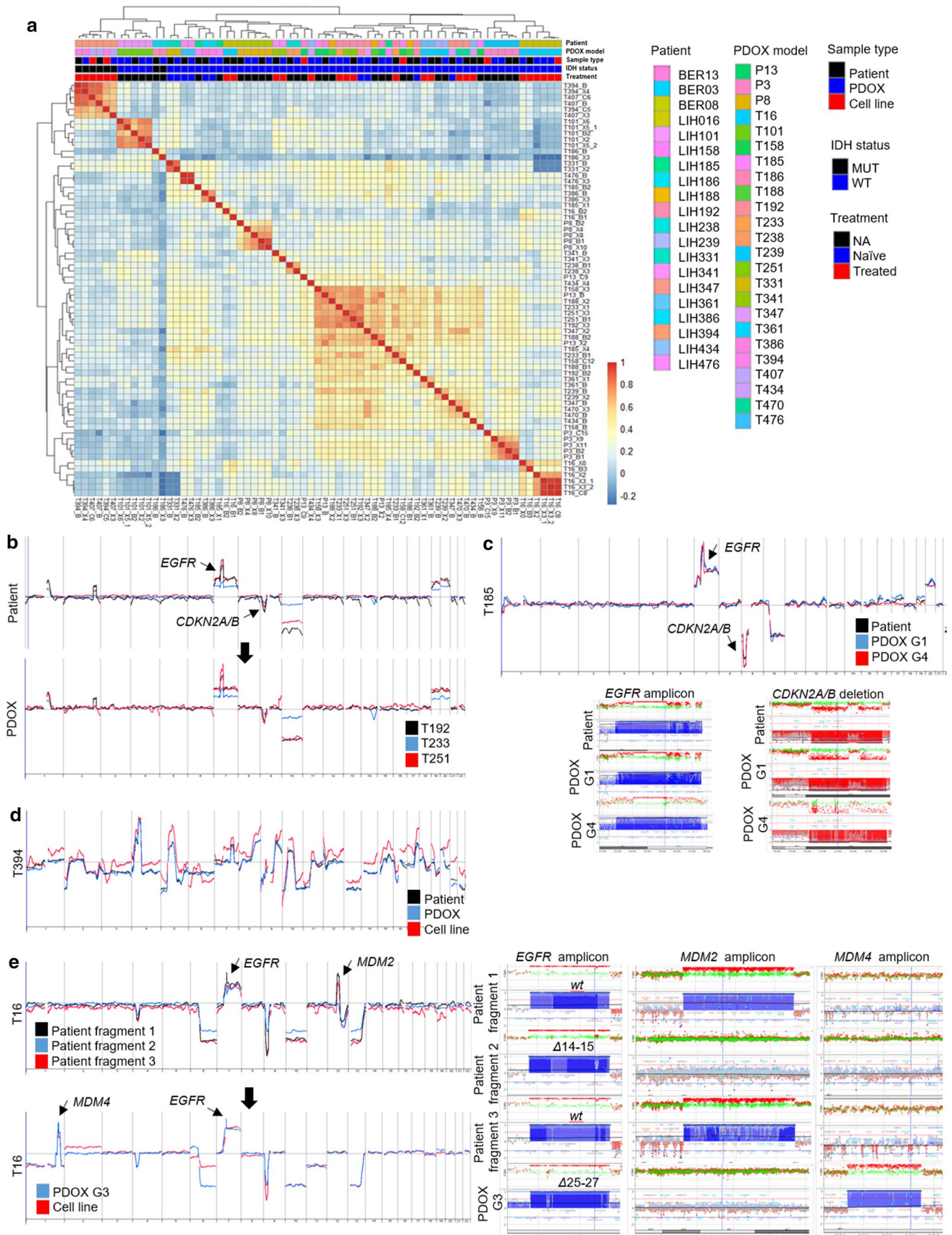


**Fig. 2** Recapitulation of copy number aberrations in PDOXs. **a** Pearson correlation between patient tumors, PDOXs, and cell lines derived based on array-CGH genetic profiles (B, patient; X, PDOX; C, cell line; adjacent numbers correspond to passage in vivo or in vitro respectively). For statistics see Supplementary Fig. 2b, online resource. **b** Array-CGH profiles of longitudinal samples (T192–T233–T251) of patient LIH0192 showing retention of genetic aberrations upon recurrence after treatment (radio + chemotherapy). The same profiles were recapitulated in PDOXs. **c** Example of an array-CGH profile of a GBM patient and corresponding PDOX model (T185 generation 1 and 4). No major changes were detected upon serial xenotransplantation. Identical chromosomal breakpoints are shown for *EGFR* amplicon and *CDKN2A/B* homozygous deletion. See more examples in Supplementary Fig. 2 and Supplementary Table 3, online resource. **d** Example of an IDH1mut glioma patient and corresponding PDOX and cell line showing high genome complexity. Patient was treated with radiotherapy before surgery. **e** Array-CGH profiles of 3 pieces of the same tumor (T16) from patient LIH0016 revealing intratumoral genetic heterogeneity (left panels). T16 PDOX and cell line were derived from additional *MDM4/EGFR* $\Delta$ 25–27-amplified clone. Right panels show the different amplicons in patient tumor fragments and PDOX

of 3D organoid structures from sorted cells. Comparison of tumors derived from these two types of organoids showed no significant difference in survival over serial transplantations (Supplementary Fig. 1g, online resource). The resulting tumors appeared histologically similar, with the expected level of invasion and the presence of an abnormal vasculature. This shows that tumors quickly adapt to the new microenvironment and recreate their niche in the brain by recruiting host-derived TME at each passage.

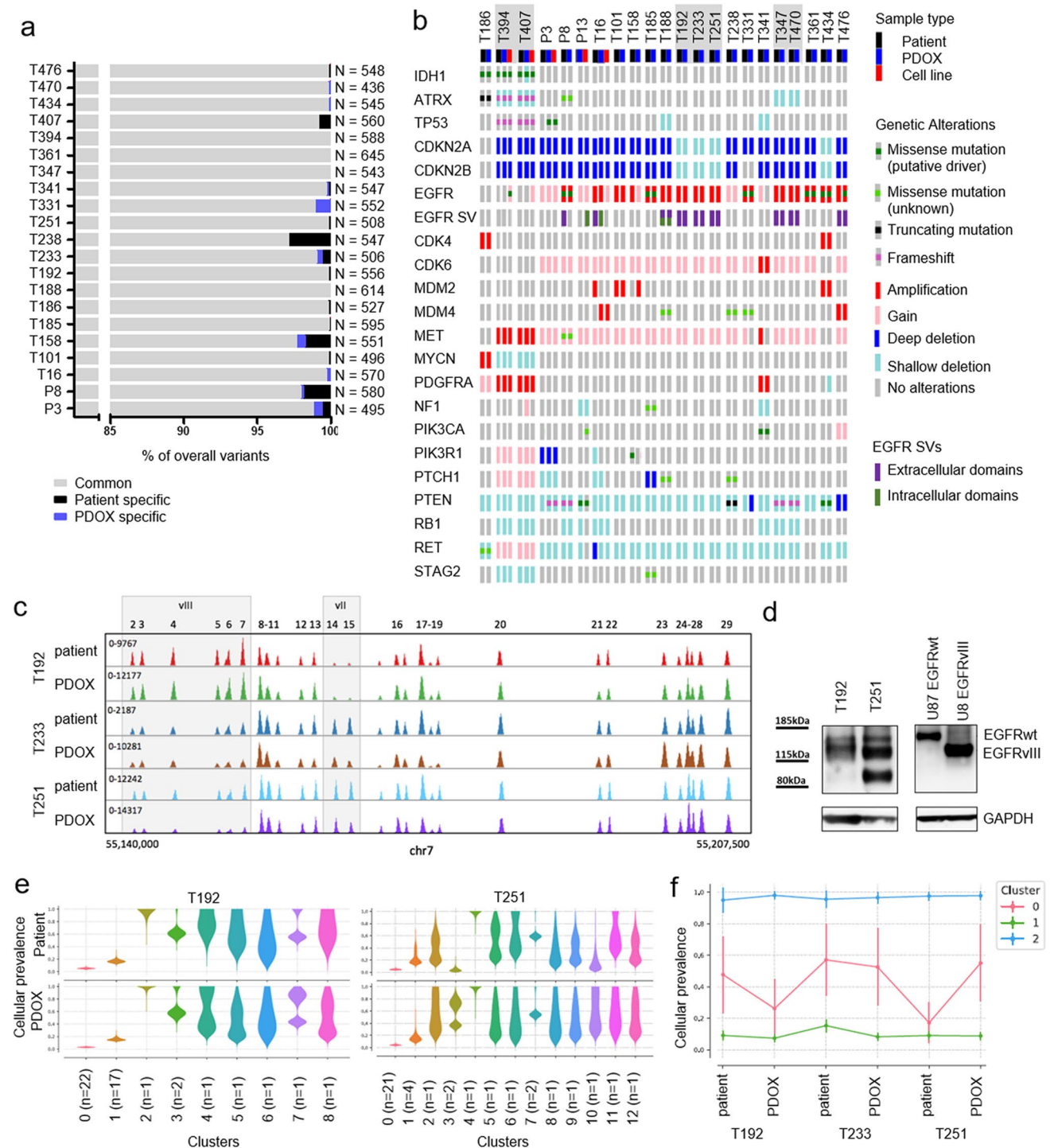
### Copy number alterations (CNAs) are well preserved in glioma PDOXs

Glial tumors display considerable genetic heterogeneity, with both inter- and intratumoral differences [91]. At the DNA ploidy level, we have previously shown that GBMs present as either mono- or polygenomic tumors where aneuploidy represents a late event in GBM evolution [92]. We found that the PDOXs retain the patient tumor ploidy states and that both pseudodiploid and aneuploid clones could be propagated by serial implantation (Supplementary Table 1, online resource). This is in contrast to long term cultures, where GSC lines of pseudodiploid tumors undergo additional aneuploidization at early passages (Supplementary Fig. 2a, online resource). By array-CGH, we show that at scale CNAs of the parental tumors were maintained with high fidelity in organoids and PDOXs both at low and high generations (Fig. 2a, Supplementary Fig. 2b, c, Supplementary Table 3, online resource). PDOXs clustered next to or in close proximity to their parental tumors. This was also true for longitudinal gliomas, where similar genomic profiles were seen in recurrent tumors after treatment (Fig. 2b, Supplementary Fig. 2d, online resource). Genomic aberrations were also assessed and confirmed by DNA Infinium

Methylation EPIC arrays (Supplementary Table 3, online resource). Most GBM patients harbored classical genetic hallmarks, such as chromosome 7 gain, chromosome 10 loss and *CDKN2A/B* deletion, which were all retained in PDOXs. This is in contrast to subcutaneous PDXs, where classical GBM CNAs were reported to be lost [7]. Moreover, focal amplicons (e.g., *EGFR*, *MDM2*, *MDM4*, *PDGFRA*, *MET*, *CDK4/6*) with the exact same breakpoints were maintained in PDOXs over generations (Fig. 2c, Supplementary Fig. 2c, online resource). IDH1mut gliomas, of which PDOXs could be established, displayed a remarkable genomic complexity (Fig. 2d, Supplementary Tables 1, 3, online resource).

### Rare genetic discrepancies reflect intratumor heterogeneity and tumor-specific evolution

It has been suggested that tumors may undergo mouse-specific tumor evolution in subcutaneous PDXs [7]. Here, in our orthotopic xenografts, we only detected minor differences between PDOXs and patients, which could largely be explained by clonal heterogeneity of the parental tumor, particularly at the level of focal amplifications known to be subclonal [45]. E.g., patient tumor T16 displayed intratumor genetic heterogeneity, where differences in gene amplicons for *EGFR* and *MDM2* were detected in different tissue fragments dissected from the tumor core (Fig. 2e). Yet another fragment carrying *MDM4* and *EGFR* amplification with  $\Delta$ 25–27 structural variant generated the initial 3D organoids and was further propagated in vivo over subsequent passages. This was similar for PDOXs T341, P8 and T158 (Supplementary Fig. 2e, g, Supplementary Table 3, online resource). These changes are most likely caused by tissue sampling bias and selection of specific subclones upon engraftment. Occasionally, we observed acquisition of additional glioma-specific CNAs in later generations (e.g., +Chr16 and –Chr 6 in PDOX T101 G6, Supplementary Fig. 2c, online resource; -1p21.1-p31.2 in PDOX P13, Supplementary Fig. 2i, online resource) in line with continuous tumor evolution over time. Of note, these rare events occurred in individual tumors and always represented known genetic aberrations in gliomas. We did not detect common genetic modifications across the cohort which could be linked to tumor growth in the mouse microenvironment, as has been suggested for subcutaneous PDX [7]. Loss or acquisition of new aberrations was much more common in cultured GSC lines (Fig. 2e, Supplementary Fig. 2g–i, Supplementary Table 3, online resource), including loss of *EGFR* gene amplification and protein expression (Supplementary Fig. 2j, online resource), as noted previously [66].



## PDOXs recapitulate glioma driver mutations and genetic heterogeneity

To further assess the mutational content and clonal architecture of patient tissues and matching organoids and PDOXs, we applied targeted DNA sequencing to identify rare variants in disease associated genes using an extended glioma-specific diagnostic panel (up to 234 genes) [85]. Overall

the PDOX models showed excellent recapitulation of the genetic variants identified in the patient tumors (Fig. 3a, b). The rare differences were mainly due to variants detected in patient tumors, but not in PDOXs tissues. These ‘lost’ variants were situated within chromosome regions deleted in the tumor and often had an allele frequency < 50 % (Supplementary Table 4, online resource), suggesting that these were germline variants with allelic loss in the tumor and



**Fig. 3** Recapitulation of DNA mutations and structural variants in PDOXs. **a** Recapitulation of overall variants determined by targeted sequencing. PDOXs were compared to respective patient tumors. The number of total variants detected for each patient tumor and PDOXs is displayed. **b** Summary of glioma specific somatic alterations including copy-number changes and mutations in patients and their derivative preclinical models. Samples highlighted in gray represent longitudinal PDOXs. **c** Example of longitudinal GBM samples (T192-T233-T251) of patient LIH0192 showing altered clonal distribution of *EGFR* structural variant *vII* to *vIII* upon relapse, which is recapitulated in the respective PDOXs. Distinct *EGFR* genomic regions deleted in respective variants are depicted. **d** Western blot against EGFR (cocktail antibody recognizing wild-type (wt) and structural variants) confirms protein expression of EGFRwt as well as the respective structural variants *EGFRvII* (in T192) and *vIII* (in T251) with decreased molecular weight. U87 cells overexpressing EGFRwt and *EGFRvIII* are shown for size reference. **e** Cellular prevalence estimates from PyClone representing clonal populations detected in longitudinal patient tumors and respective PDOXs. Examples shown for T192 and T251. Each cluster of mutations was computationally inferred to reflect a subclone. Number of genetic variants contributing to each clone is depicted. **f** Cellular prevalence estimates from PyClone representing clonal subpopulations detected in longitudinal patient LIH0192 and its respective PDOXs. Each line represents a cluster of mutations computationally inferred to reflect a subclone. Only genetic variants detected in all samples were considered for analysis

likely originate from normal human tissue (TME) present in the patients tumor, but not in the PDOX models. Only a handful of genetic variants private to PDOXs were detected and nearly all were located in noncoding regions (Fig. 3a, Supplementary Table 4, online resource). In comparison, PDOX-derived cell lines showed acquisition of further new variants in cultures (Supplementary Fig. 3a, online resource).

Targeted sequencing confirmed identified copy-number alterations and further revealed specific mutations characteristic for gliomas (Fig. 3b, Supplementary Table 5, online resource). Assessed IDH1mut gliomas (PDOX and parental tumor) carried mutations in *ATRX* and *TP53* genes, in line with the molecular diagnosis of astrocytomas obtained by CpG methylation profiling [20] (Fig. 1b). Digital PCR confirmed the presence of wild-type and *R132H* mutated *IDH1* alleles in PDOXs, although variations in ratio were observed probably due to TME signal in patient tumors and tumor aneuploidy (Supplementary Fig. 3b, online resource). In line with previous reports [68, 88], in vitro GSC cultures drastically reduced *IDH1* wild-type allele frequency in T394NS, i.e., cells had lost wild-type *IDH1* by passage 10, whereas T407NS retained still 20% of the wild-type *IDH1* allele at passage 13. This was combined with an acquisition of several new variants (Supplementary Fig. 3a, online resource). IDHwt GBM PDOXs retained common glioma mutations, including *EGFR*, *MDM4*, *PTEN*, *PIK3CA*, and *PTCH1* (Fig. 3b). One PDOX (P13) carried an *IDH2* missense mutation (*W244R*) of unknown significance, which has been described in the normal population (rs780131378)

and is probably a rare private germline variant. It was not associated with increased 2HG production (Supplementary Table 5, online resource), and thus the tumor was considered as IDHwt. The *EGFR* gene status was remarkably well preserved in the PDOXs. *EGFR* point mutations were detected in the extracellular domain (*A289T*, *G598V*, *F254I*, *R108K*), and co-occurred with *EGFR* amplification. *EGFR* structural variants were present in the extracellular and/or intracellular domains, such as  $\Delta 2-7$  (*EGFRvIII*),  $\Delta 2-15$ ,  $\Delta 6-7$ ,  $\Delta 14-15$  (*EGFRvII*), and  $\Delta 25-27$  (Supplementary Table 5, online resource). Notably, in agreement with a previous report [9], PDOX P8 displaying *EGFR A289T* was one of the most invasive and proliferative GBM.

In general, our matched longitudinal models retained similar coding variants upon recurrence (Fig. 3b). Interestingly, LIH0192 patient tumor underwent heterogeneous complex structural rearrangements leading to a shift from *EGFRvII* to *EGFRvIII* upon relapse. These changes led to different EGFR protein expression and were retained in the respective PDOXs (Fig. 3c, d). LIH0347 patient-derived longitudinal PDOXs retained *EGFR* $\Delta 2-15$ , which also showed immunoreactivity to *EGFRvIII* antibodies (Supplementary Fig. 3c, online resource).

We further used PyClone to follow the clonal dynamics upon engraftment of patient tissues and were able to demonstrate that PDOXs retain genetic heterogeneity at the subclonal level (Fig. 3e, Supplementary Fig. 3d, online resource). Subclonal fractions were also retained in longitudinal models of patients LIH0192 and LIH0347, although certain fluctuations in cellular prevalence were observed (Fig. 3f, Supplementary Fig. 3e, online resource). Interestingly, we also observed evolutionary dynamics in *EGFR* amplicons (Supplementary Fig. 3f, online resource), arising most probably from evolutionary trajectories of extra-chromosomal double minutes [35]. In summary, glioma PDOXs largely recapitulate genetic aberrations and genetic heterogeneity of the parental tumors. Rare newly acquired genetic features in PDOXs recapitulate glioma mutations known in patients, suggesting that growth of human tumors in the rodent brain can serve as a proxy for ongoing genetic evolution in the brain microenvironment. This is in contrast to in vitro passaging of glioma cells which regularly leads to additional genetic aberrations which are not glioma specific.

### Tumor intrinsic epigenetic profiles are preserved in PDOXs

Cancer-specific DNA methylation patterns are important drivers of gene expression and have been recognized as a preferred prognostic biomarker used for brain tumor subtyping [20, 22, 79]. Correlation analysis and principal component analysis (PCA) based on EPIC and 450K Illumina DNA methylation arrays showed an overall good

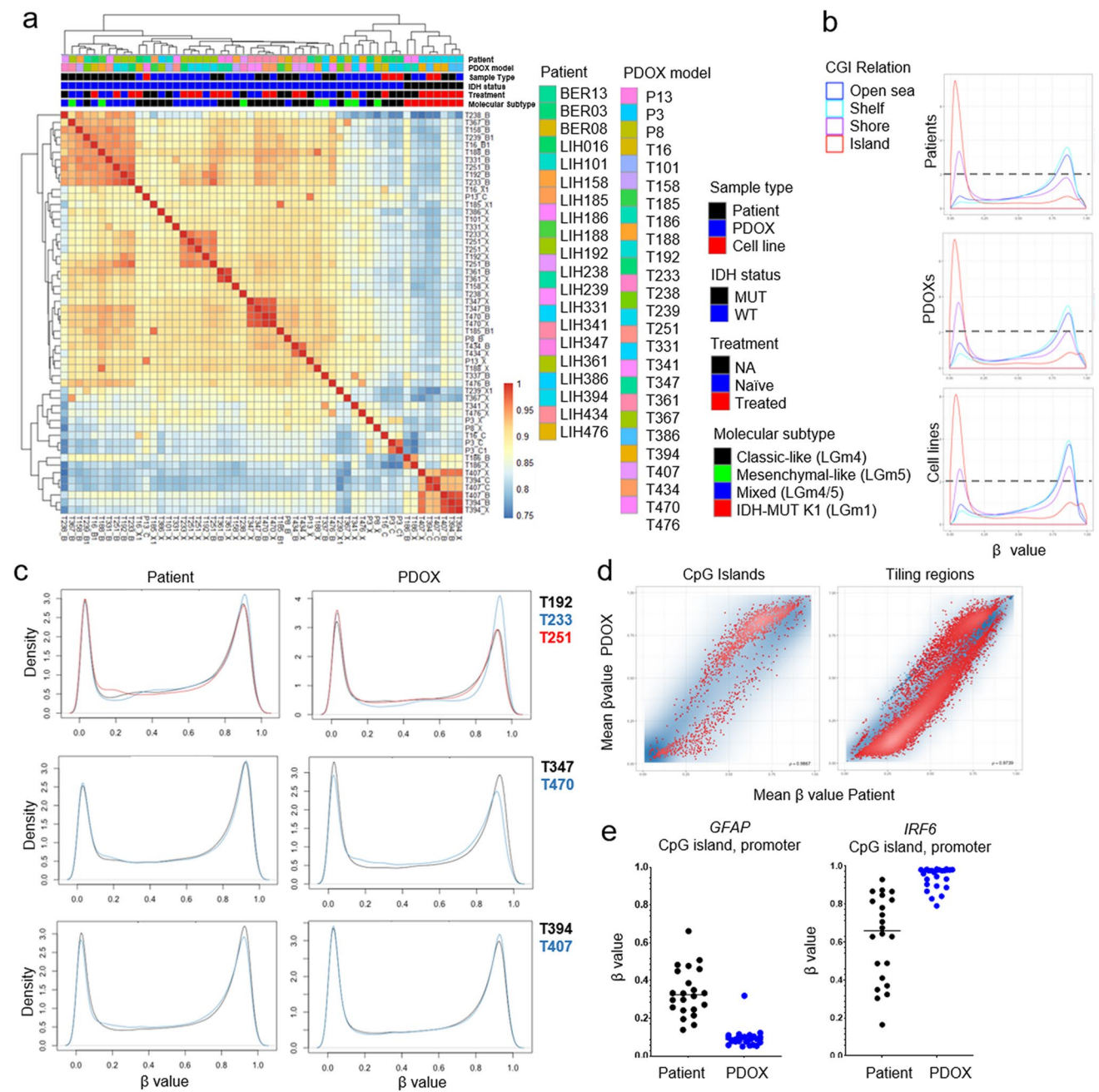


**Fig. 4** DNA methylation profiling. **a** Pearson correlation of DNA methylation profiles between glioma patient samples, PDOXs and cell lines derived thereof based on 450 k and EPIC arrays (B, patient; X, PDOX; C, cell line, overlapping regions between arrays only). For statistics see Supplementary Fig. 4a, online resource. **b** Global beta-value distributions are very similar between patient samples and PDOXs. Cell lines displayed an increased DNA methylation at open sea, shelf, and shore regions. **c** Beta-value distributions are very similar upon tumor recurrence and are recapitulated in corresponding PDOXs. Examples are shown for longitudinal samples of patients

LIH0192, LIH0347, and LIH0394, the latter being IDH1mut. **d** Mean beta-value distribution in patients and PDOXs show increased methylation in a subset of CpG islands and decreased methylation of tiling regions in PDOXs. CpG sites with FDR < 0.05 are displayed in red, remaining probes are shown in blue. **e** Examples of hypo- and hypermethylated CpG islands in PDOXs. *GFAP* is widely expressed in GBM, whereas *IRF6* is involved in innate immune response. Differentially methylated sites are changing from hemi-methylated in patient tumors to either unmethylated (*GFAP*) or methylated (*IRF6*) status in PDOXs

correlation between patient tumors and PDOXs (Fig. 4a, Supplementary Fig. 4a, online resource), where samples clustered based on IDH status. Although sample type also

contributed to the source of variation in the cohort, the IDH status was the main source of variation (Supplementary Fig. 4b, online resource). IDH1mut gliomas displayed

divergent DNA methylation of specific CpG islands compared to IDHwt gliomas (Supplementary Fig. 4c, online resource). Yet, G-CIMP-low subtype dominated our IDH1mut patient tumors and PDOXs (Supplementary Table 6, online resource), presumably in line with their increased aggressiveness [33]. The beta-value distributions were very similar between PDOXs and parental tumors, whereas GSC lines displayed increased DNA methylation at open sea, shelf, and shore genomic regions (Fig. 4b). This was supported by PCA analysis showing a lower similarity of GSC lines to patient tumors in comparison to PDOXs (Supplementary Fig. 4a, online resource). This was true for IDH1wt and mutated cell lines (Supplementary Fig. 4a, d, online resource). Importantly, the *MGMT* promoter DNA methylation status was preserved between PDOX and parental tumor in all but two PDOXs (Supplementary Table 6, online resource). Global DNA methylation profiles based on beta-value distributions were also well preserved in longitudinal glioma samples between each other and with their respective PDOXs. Overall, most tumors retained the same DNA methylation profile upon recurrence (Fig. 4c), including *MGMT* promoter methylation status (Supplementary Table 6, online resource), although differences at individual CpG sites are possible.

Statistical analysis of paired methylation profiles revealed only minor changes between patient tumors and respective PDOXs (Limma, FDR < 0.01). Only 35 individual CpG sites showed differences in mean methylation beta values above 0.4, corresponding to an essential switch in DNA methylation status, but none were gene annotated CpGs. A partial change of DNA methylation levels (beta value difference 0.2–0.4) was observed at CpG sites of 226 CpG islands, 89 promoters, 74 gene bodies and 943 tiling regions. Most sites that were demethylated in PDOX corresponded to tiling regions that changed from hemi- to unmethylated (894/943, Fig. 4d), pointing towards global hypomethylation characteristic for high-grade glioma [22]. This was also true for certain gene promoters specific to GBM cells (e.g., *GFAP*, Fig. 4e). An increase towards fully methylated CpG sites was observed typically at CpG islands (196/226, Fig. 4d), including promoters of genes expressed classically by the TME (e.g., *IRF6* for immune cells, Fig. 4e), reflecting the impact of non-neoplastic cells on methylation profiling [56]. Accordingly, the molecular classification based on previously defined DNA methylation classes [20, 22, 33] was well retained in PDOXs (Fig. 4a, Supplementary Table 6, online resource). Class switches between patient and PDOX occurred from mesenchymal-like to classic-like tumors (LGm5 to LGm4, mesenchymal to RTK II class, Supplementary Table 6, online resource), in line with the influence of the TME on DNA methylation profiles as has also been shown for gene expression signatures [112]. GSC cell lines displayed more divergent DNA methylation profiles with

increased DNA methylation levels (Fig. 4a, b) and were not clearly classified (Supplementary Table 6, online resource). Although we did not detect a link between treatment history of patient tumors and molecular subtypes, more data will be required in the future to perform meaningful statistical analyses.

### Gene expression analysis reveals close resemblance between patient tumors and PDOXs

To determine to what extent gene expression profiles of parental tumors are retained in glioma PDOXs, we performed genome-wide transcript analysis using human-specific microarrays (Fig. 5a). In parallel, we analyzed cell cultures and corresponding intracranial xenografts from GSC (NCH421k, NCH644) and adherent cell lines (U87, U251). Unsupervised hierarchical cluster and PCA analyses revealed close resemblance of PDOXs to corresponding patient tumors, although higher similarity of samples of the same type was observed (Fig. 5a, Supplementary Fig. 5a, online resource). Cell lines and their xenografts were more dissimilar and clustered according to their origin, in line with a higher cellular selection and adaptation in long term in vitro cultures. Transcriptomic profiles of PDOXs also displayed strongest similarity to GBMs from the TCGA cohort [19] (Supplementary Fig. 5b, online resource). Analysis of transcriptomic subtypes revealed differences when using the original molecular signatures proposed by Verhaak et al. [107]. However, with the recent tumor-intrinsic classification aimed at reducing the influence of TME [112], the subtyping remained constant (Supplementary Table 7, online resource), suggesting that transcriptomic differences between patient tumors and PDOXs arise from TME-associated gene expression. Cell lines retained transcriptomic subtypes were retained upon in vivo growth. Analysis of differentially expressed genes between PDOXs and parental tumors (2-way ANOVA, FDR < 0.01, absFC ≥ 2) revealed an increase in tumor intrinsic signals such as cell cycle and DNA repair (Fig. 5b), which was most prominent in highly proliferative PDOXs (P3, P8, P13, Fig. 5c). Genes down-regulated in PDOXs were associated with TME processes, i.e., immune response, angiogenesis and macrophage activation (Fig. 5b, c). Specific markers of human TME components such as endothelial cells (*VWF*, *KDR*), microglia/macrophages (*ITGAX*, *AIF1*, *CD68*), pericytes/vascular smooth muscle cells (*PDGFRB*, *ACTA2*) and hematopoietic cells (*CTLA4*, *CD4*, *PTPRC*) were depleted in PDOXs (Fig. 5c). This included also *ABCBI* and *ABCG2*, which we have previously shown to be restricted to brain endothelial cells in human GBM [47]. The general depletion of human TME transcriptome upon xenografting was confirmed by independent component analysis (Fig. 5d) and flow cytometry (Fig. 5e). Interpatient differences were retained in PDOXs,

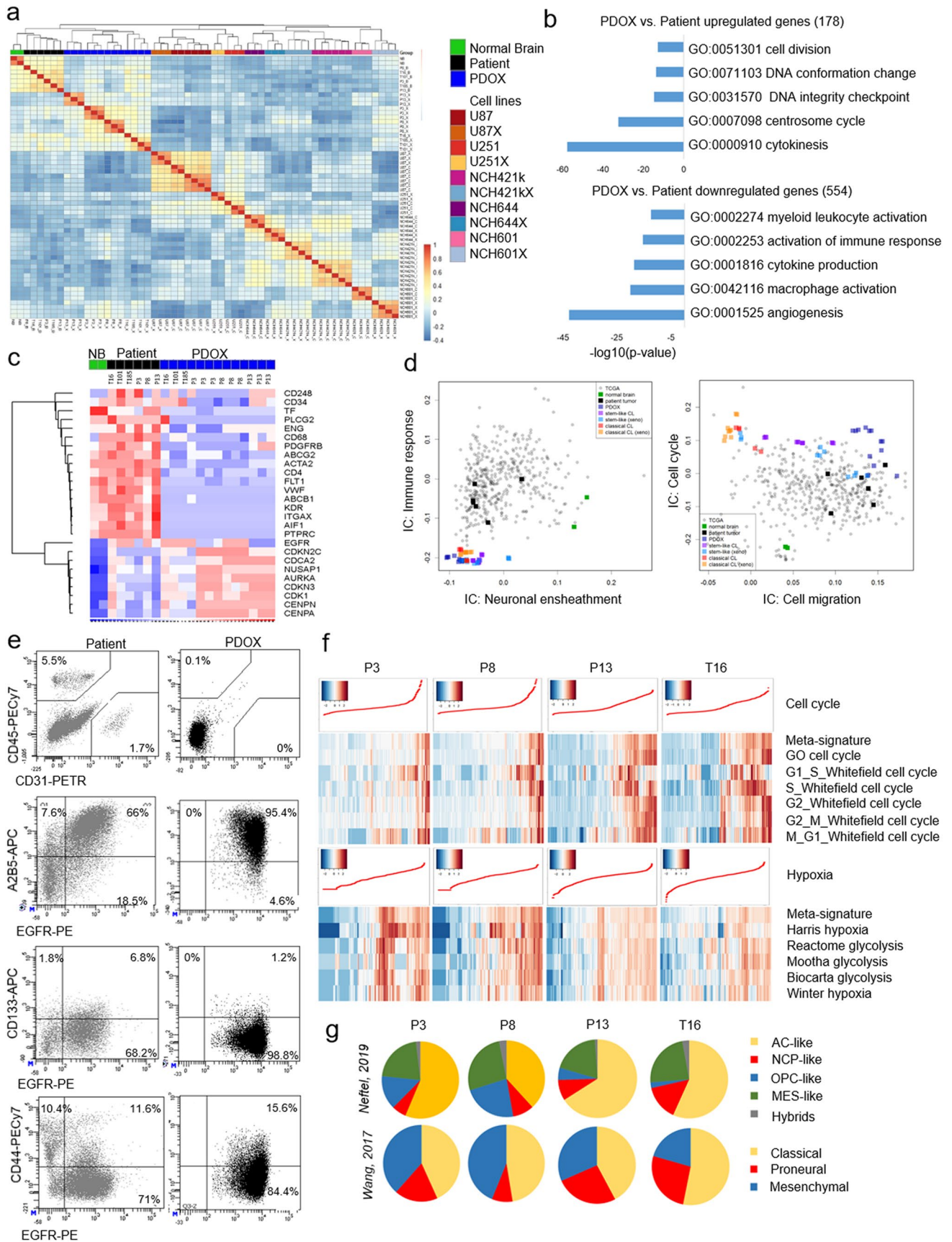


**Fig. 5** Transcriptomic profiles and intratumoral heterogeneity. **a** Pearson's correlation indicating similarity of genome-wide gene expression profiles between normal human brain, glioma patient samples, PDOXs, GSC lines (NCH421k, NCH644) and classical glioma lines (U87, U251) grown in vitro or as xenograft ('X'). Human specific arrays were applied for transcriptome analysis. **b** Summary of main GO terms characterizing genes differentially present in PDOXs (FRD  $\leq 0.01$ , ab(FC)  $\geq 2$ , Limma). **c** Heatmap representing gene expression levels for a selection of classical TME and cell cycle markers in normal brain (NB), patients and respective PDOXs. **d** Independent component analysis showing depleted transcriptomic signals associated with immune response and neuronal ensheathment in PDOXs and cell lines. Cell cycle independent component (IC) was the highest in PDOXs and cell lines, cell migration-associated IC was the highest in patients and PDOXs. **e** Flow cytometric analysis to detect human cell subpopulations in patient samples and respective PDOXs. Examples are shown for PDOX T331 expressing EGFR in tumor cells. **f** Single cell signatures showing the presence of human tumor cells in distinct phases of cell cycle and hypoxic gradient in PDOXs. **g** Assessment of GBM cellular states [77] and TCGA GBM subtypes [112] at single cell level in PDOX tumor cells

e.g., *EGFR* expression was maintained at similar levels as in patients (Fig. 5c). We did not detect an upregulation of specific molecular pathways linked to stemness (i.e., cancer stem-like profiles), confirming the lack of a particular selection for tumor subpopulations. Indeed, the heterogeneous expression of stem cell markers in GBM, as previously reported [36], was retained in the respective PDOXs (Fig. 5e) and remained largely stable over serial transplantations (Supplementary Fig. 5c, online resource). Transcriptomic analysis at the single cell level revealed similar proportions of cycling cells and the presence of a hypoxic gradient in PDOX (Fig. 5f) as shown for GBM patients [81]. PDOXs also recapitulated intratumoral heterogeneity and phenotypic cellular states previously described in GBM patients [77, 112] (Fig. 5g). Mouse-derived TME, which replaced human TME, showed similar cellular subpopulations as detected in patient tumors including microglia/macrophages, oligodendrocyte progenitor cells (OPCs) and astrocytes comparable to human GBM TME [31] (Supplementary Fig. 5d, online resource). In conclusion, our data show that glioma PDOXs recapitulate well tumor-intrinsic transcriptomic profiles. Differences in gene expression signatures at the bulk level can be explained by the replacement of the human TME by mouse cells undergoing GBM-specific adaptation.

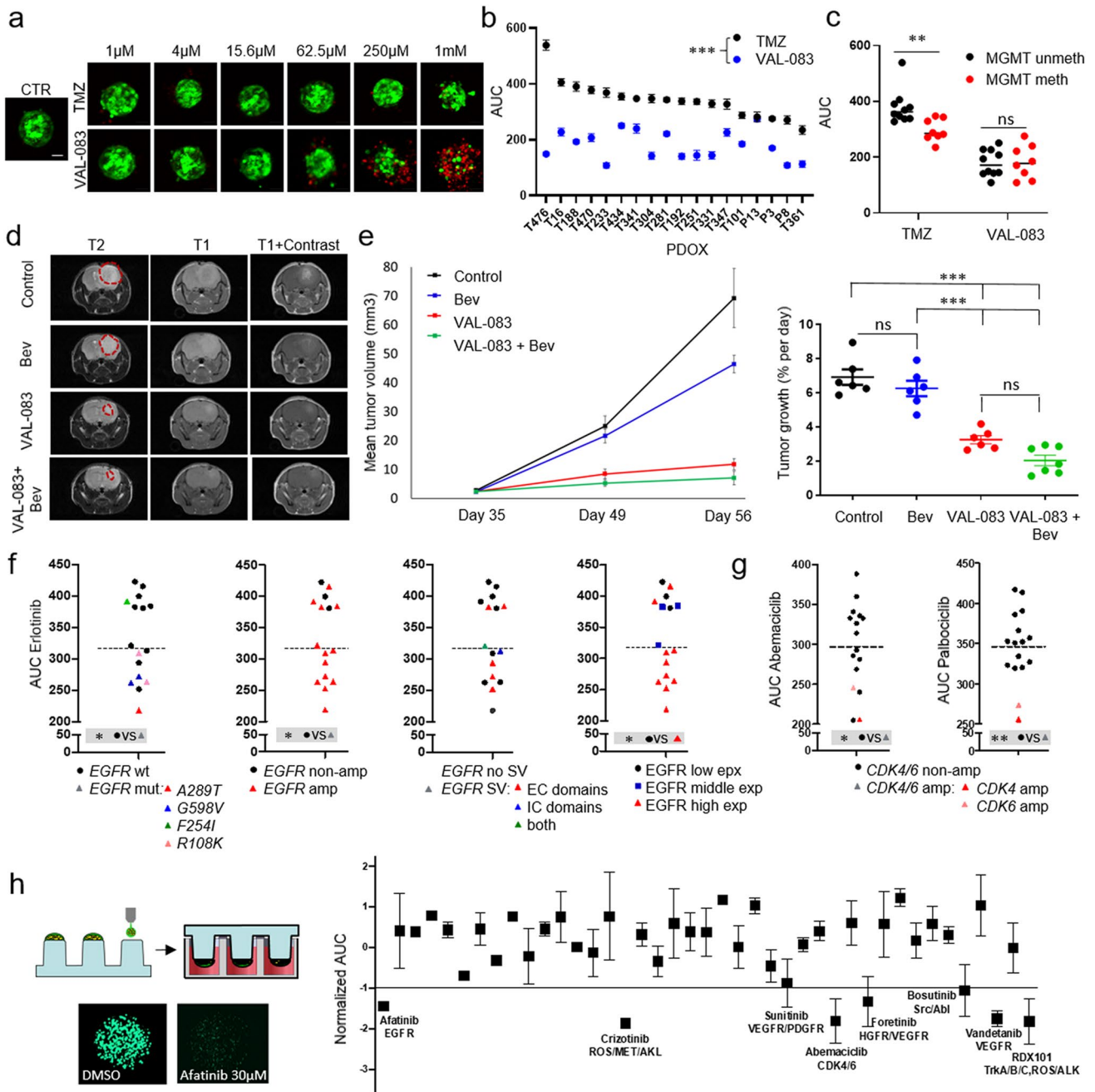
### Preclinical drug testing in PDOX-derived standardized 3D glioma organoids provides clinically relevant outcomes

The PDOX cohort described above constitutes a living biobank maintained by serial transplantation of organoids obtained through mechanical cutting of tumor tissue. This allows to expand the patient tumor in its natural brain

microenvironment, generating sufficient material for large scale preclinical drug testing. To this aim, we standardized the derivation of uniform GBM organoids amenable for reproducible drug screening. Organoids were generated from 1000 MACS-purified single tumor cells obtained from PDOXs, which were able to self-organize into 3D organoids within 72h in nonadherent conditions (Fig. 6a). This allowed for sensitive evaluation of cell viability and toxicity in a 384-well plate format (Supplementary Fig. 6a, online resource), similar to protocols described for other types of cancer organoids [44]. To assess whether PDOX-derived organoids recapitulate known mechanisms of drug sensitivity and achieve clinically relevant responses, we subjected a cohort of 18 GBM PDOXs to temozolomide (TMZ), the standard DNA-alkylating agent in clinical practice. Cell responses were calculated as the Area Under the Curve (AUC). In accordance with clinical data, GBM organoids showed only a partial response to TMZ (AUC 200–600, Fig. 6a, b, Supplementary Fig. 6b, online resource). Importantly, tumors with a methylated *MGMT* promoter appeared less resistant in comparison to *MGMT* promoter-unmethylated GBMs (Fig. 6c, Supplementary Fig. 6b, online resource). No differential response was observed between treatment-naïve organoids and organoids derived from patients previously exposed to chemoradiotherapy (Supplementary Fig. 6c, online resource).

### Dianhydrogalactitol (VAL-083) exhibits strong efficacy against GBM independent of (epi)genetic background and treatment history

We further tested dianhydrogalactitol (VAL-083), a bifunctional compound able to alkylate N<sup>7</sup>-guanine and form interstrand crosslinks and DNA double strand breaks [117]. VAL-083 is known to penetrate the blood–brain barrier and to accumulate in the cerebrospinal fluid and brain parenchyma [39]; it is currently tested in clinical trials for recurrent GBM (NCT02717962) as well as for treatment-naïve *MGMT* promoter unmethylated GBM patients (NCT03050736). In our cohort, VAL-083 was significantly more effective than TMZ (Fig. 6a, b) and the response was not dependent on *MGMT* promoter methylation status (Fig. 6c). The response was similar in treatment-naïve and relapsed organoids (Supplementary Fig. 6c, online resource), suggesting that VAL-083 is able to overcome TMZ resistance. In view of the strong efficacy of VAL-083 in the ex vivo assay we evaluated its ability to decrease tumor growth in vivo. Due to the structural similarity with glucose, we hypothesized that uptake of VAL-083 could be further enhanced under hypoxia; we therefore also applied a combination treatment with the antiangiogenic agent Bevacizumab previously shown to induce hypoxia in GBM [1, 53]. As expected, Bevacizumab treatment



did not halt tumor progression despite decreased contrast enhancement on MRI (Fig. 6d) and blood vessel normalization (Supplementary Fig. 6d, online resource). VAL-083 monotherapy led to a dramatic reduction in tumor growth (Fig. 6e), an effect which was only mildly accentuated by combined treatment. Histological assessment of tumor-containing brains confirmed the strong reduction in tumor volume upon VAL-083 treatment (Supplementary Fig. 6e, online resource). This was paralleled by an increase in

DNA damage in tumor cells, determined by H2AX phosphorylation (H2AX-P) (Supplementary Fig. 6f, online resource). Limited H2AX-P was also seen in normal brain cells close to the meninges and the subventricular zone, but to a much lower extent than in tumor cells. In summary, we show that VAL-083 has a consistently favorable drug profile against GBM; thus, representing a promising candidate for GBM treatment either alone or in combination with antiangiogenic compounds.

**Fig. 6** Drug response assessment in glioma organoids and PDOXs. **a** Drug response was evaluated in PDOX-derived organoids with standardized size (green, viable; red, dead cells). Representative images are shown for TMZ and VAL-083 treatment of T434-derived organoids. Scale bar = 50  $\mu\text{m}$ . **b** Quantification of AUC upon exposure to TMZ and VAL-083. Mean AUC  $\pm$  SEM is shown for each model. Experiment was performed once with three technical replicates per PDOX per drug concentration. VAL-083 is generally more effective in PDOX-derived organoids in comparison to TMZ ( $***p_{\text{value}} < 0.001$ , unpaired  $t$  test). **c** Mean AUC upon exposure to TMZ and VAL-083 in *MGMT* promoter methylated and unmethylated tumors. Tumors with methylated *MGMT* promoter show enhanced response to TMZ, while response to VAL-083 is independent of the *MGMT* promoter status ( $**p_{\text{value}} < 0.01$ , unpaired  $t$  test). **d** PDOX T16 treated *in vivo* with VAL-083, Bevacizumab or a combination. Tumor progression was assessed by T1-weighted and T2-weighted MRI images ( $n = 6\text{--}7$  mice per group) prior treatment (day 35) and post treatment (day 49 and 56 equivalent of 14 and 21 days since beginning of treatment respectively). **e** Assessment of tumor progression over time reveals significant reduction of tumor growth upon VAL-083 treatment. Tumor growth rate between treatment groups was calculated during the entire study (day 35 vs. day 56,  $n = 6\text{--}7$ ,  $***p_{\text{value}} < 0.001$ ,  $**p_{\text{value}} < 0.01$ , ANOVA with Tukey's Multiple Comparison Test). **f** Quantification of AUC upon exposure to EGFR inhibitor Erlotinib showing higher sensitivity in *EGFR* mutated tumors (vs *EGFR* wild type) and in *EGFR* amplified tumors (vs *EGFR* nonamplified). This is also recapitulated at the level of *EGFR* protein expression. No significant effect is seen for tumors with or without *EGFR* variants. ( $*p_{\text{value}} < 0.05$ , unpaired  $t$  test); wt, wild type; mut, mutated; Amp, amplified; SV, structural variant; EC, extracellular domains; IC, intracellular domains; exp, expression. **g** Quantification of AUC upon exposure to CDK4/6 inhibitors Palbociclib and Abemaciclib shows higher sensitivity of *CDK4* and *CDK6* amplified tumors (vs nonamplified tumors). ( $*p_{\text{value}} < 0.05$ ,  $**p_{\text{value}} < 0.01$ , unpaired  $t$  test). For **f**–**g** experiments were performed twice with 3 technical replicates each. See Supplementary Table 8 for mean AUC  $\pm$  SEM. **h** High-throughput screening with 42 FDA-approved drug library in PDOX T434. Drug response data are displayed as normalized AUC  $\pm$  SEM, ( $n = 2$ ), '–1' value is indicated as a threshold for strongest hits

### PDOX-derived organoids are amenable to high-throughput drug screening for precision medicine

To evaluate the potential for personalized treatment regimens of our models, we functionally assessed the response against a set of *EGFR*/*ErbB* small-molecule tyrosine kinase inhibitors (Erlotinib, Gefitinib, AZD3759, AG490, and Daphtenin) and CDK4/6 inhibitors (Abemaciclib, Palbociclib) with varying specificity in 16 PDOX-derived organoids with variable genetic makeup of these pathways. The inability to preserve gene amplification and *EGFR* structural variants in most cell culture models including GSCs [66], did so far not allow for accurate personalized preclinical studies. Our testing group included GBM with different status of *CDK4*, *CDK6*, and *EGFR* amplification, *EGFR* genetic variants and point mutations (Fig. 3b, Supplementary Table 5, online resource). The responses against *EGFR* inhibitors were highly variable across patient organoids (Fig. 6f, Supplementary Fig. 6g,

online resource). In contrast to kinase domain mutations found in lung cancer, glioma-specific extracellular domain mutants are known to respond poorly to *EGFR* inhibitors [64]. Still, we found that GBMs carrying *EGFR* mutations, except for *EGFR F254I* (PDOX T434), were more sensitive to Erlotinib and AZD3759, but not to the other *EGFR* inhibitors, Gefitinib, AG490 and Daphtenin (Fig. 6f and Supplementary Fig. 6g, online resource). This is in accordance with the fact that *EGFR R108K*, *G598V*, and *A289T* are missense mutations leading to a gain-of-function, shown previously to sensitize tumors to Erlotinib [63]. The role of *EGFR F254I* is currently unclear. *EGFR* amplification and corresponding high protein expression also had an impact on the sensitivity to Erlotinib and AZD3759, where nonamplified tumors with low protein expression were most resistant. *EGFR* structural variants did not sensitize tumors in our cohort to any of the five compounds. Similarly, tumors carrying *CDK4* (PDOX T434) and *CDK6* (PDOX T341) amplification were most sensitive to CDK4/6 inhibitors Palbociclib and Abemaciclib (Fig. 6g).

Finally, we performed a proof-of-concept study on PDOX-derived organoids for high-throughput drug screening using the cell printing technology based on the ASFA Spotter ST [37]. PDOX T434 derived GBM cells were dispensed onto pillars (1000 cells per pillar), embedded into alginate drops and allowed to reform 3D organoids (Fig. 6h). A library of 42 FDA-approved drugs was then applied for 7 days and response was assessed via a High Content imaging system (CV 8000) recognizing viable cells. To select the strongest hits, we applied normalized AUCs (Z score,  $-1$  threshold) [64]. The screen showed similar responses as the 384-well plate protocol (Supplementary Fig. 6h, online resource), and confirmed sensitivity of T434 tumor cells to Abemaciclib and resistance to Erlotinib and Gefitinib. Interestingly, it revealed sensitivity to several other inhibitors, including Afatinib,—a second-generation *EGFR* inhibitor. In summary, we show that PDOX-derived GBM organoids display clinically relevant drug responses and can be applied for personalized drug screening in a high-throughput manner.

### Discussion

Although major discoveries can be performed directly on patient tumors, biological material is restricted, generally limiting such studies to descriptive analyses and low-throughput preclinical assays. Here we present a living tumor biobank that encompasses the clinical diversity of high-grade diffuse gliomas. Over 160 organoids and 40 PDOX models were established from treatment-naïve glioma patients and patients that underwent standard-of-care, of which 15 represent paired longitudinal models. Glioma organoids grown in PDOX, combines the generation of a

powerful *in vivo* model for precision oncology with the expansion of patient tumor material in an appropriate TME setting not possible *in vitro*. Our PDOX cohort contains tumors of varying genetic and molecular background, and represents a unique tool for drug screening, functional studies and *in vivo* drug efficacy studies. We show that glioma PDOXs recapitulate (1) glioma tissue architecture, including features of angiogenesis and invasion, (2) genetic variants and CNAs, including rare gene amplifications (3) epigenetic and transcriptomic tumor intrinsic signatures, (4) intratumoral genetic, transcriptomic, and stem-cell-associated heterogeneity, (5) clinically relevant drug responses. Our models and associated molecular data are openly shared and available at the PDXfinder portal (<https://www.pdxfinder.org/>) and via the EurOPDX consortium (<https://www.europdx.eu/>). They represent a robust tool for reliable expansion of patient tumor material while maintaining close identity with the parental tumors, allowing for high-throughput drug testing and precision medicine.

Most available glioma PDX models are established and maintained through subcutaneous implantation of tumor fragments [21, 106], where the long term impact of a non-brain TME is unclear. Orthotopic GBM xenografts usually rely on single cell dissociation followed by *in vitro* cultures as GSCs (BTICs) prior to xenotransplantation [21, 35, 49, 52, 108], where cultures are often maintained for unspecified time and passage number. To minimize the loss of tissue architecture and clonal heterogeneity, we use organoids from mechanically minced glioma tissue, only briefly maintained in culture without any *in vitro* passaging. In order to maintain the heterogeneous nature of the primary tumor within self-organizing organoids, we did not try to achieve indefinite growth of organoids *in vitro* [49, 51], instead we orthotopic xenografting for tissue expansion and maintenance. We find that most GBMs and lower grade gliomas give rise to short-term organoids. Successful PDOX establishment enriches for high-grade tumors, including IDHwt GBMs and IDH1mut gliomas grades III and IV. This is in concordance with the general selection of aggressive tumors upon PDX generation in different tumor types, including pediatric brain tumors [13]. So far, only a handful of IDH1mut glioma models have been described, which all suffer from poor reproducibility, a long development time and/or changes in *IDH1* status [55, 69, 75, 99, 106, 109]. Successful IDH1mut models in our cohort were defined molecularly as high-grade astrocytomas with abundant chromosomal aberrations, *CDKN2A/B* loss, *ATRX*, and *TP53* mutations and G-CIMP-low signature. These molecular features correspond to the most aggressive IDH1mut gliomas [5, 33, 109]. Importantly, our models retain *R132H IDH1* heterozygosity and efficient production of 2HG [43]. *In vitro* cultures derived from these tumors either died or led to depletion of the wild-type *IDH1* allele, in line with previous reports [68, 104], suggesting that

IDH1mut gliomas require components of the brain microenvironment to maintain their growth. Importantly, our fully annotated cohort displays a wide variety of genetic features not recapitulated in other models (e.g., *EGFR* and *PDGFRA* amplification), thus reflecting the wide interpatient heterogeneity of high-grade gliomas. Our PDOX biobank also contains 15 unique paired models derived from the same patients at initial diagnosis and upon disease relapse.

The recapitulation of histopathological features of gliomas has been challenging with classical serum-grown cell lines, as they largely lose the characteristic invasive potential of diffuse gliomas upon xenotransplantation [28, 71]. Infiltrative growth is maintained in all our PDOXs, although the extent of typical glioma features, including invasion, angiogenesis, and proliferation rate can greatly vary across models, likely reflecting interpatient heterogeneity. We find that prominent angiogenic features along with pseudopalisading necrosis are rare in mice compared to rats, which may arise from differences in brain size and/or in molecular interaction between species. This suggests that for studies addressing aspects of angiogenesis, hypoxia, and blood–brain barrier, rat PDOX models may be more appropriate. Others have also reported gradients of invasive and angiogenic features across GBM xenografts, with limited endothelial proliferation and necrosis in mouse brains [106, 109], while large subcutaneous tumors display extensive angiogenesis [106].

We have previously shown that GBM organoids and corresponding PDOXs faithfully retain tumor cell ploidy [92]. Here we demonstrate that glioma organoids and PDOXs accurately maintain distinct genetic backgrounds of parental tumors, including gene amplifications of *EGFR*, *PDGFRA*, *MET*, *MDM2/4*, and *CDK4/6*, which are difficult to derive and preserve *in vitro* [66, 88]. PDOXs also recapitulate complex *EGFR* variants and mutations present concomitantly with *EGFR* amplification. At scale, we found that individual genomic profiles are highly conserved in PDOXs. We did not detect major divergences in CNAs as reported for subcutaneous GBM PDXs [7]. The difference in results may be related to the subcutaneous transplantation, which may lead to a different tumor evolution than in the brain. Alternatively, it may be due to differences in data analysis, since array-CGH based CNA determination, employed by us, is known to be more accurate than CNAs inferred from gene expression profiles [115]. We further observed extensive preservation of genetic intratumoral heterogeneity, although some fluctuations in subclonal architecture were detected. Interestingly, we report a case of *EGFR* variant selection, observed both upon tumor relapse in patients as well as upon xenografting. This may be linked to high levels of *EGFR* amplification and the presence of extrachromosomal double minute structures, which are known to show evolutionary dynamics [35].

In rare cases PDOX models showed engraftment or expansion of specific genetic clones, with distinct gene



amplifications or mutations, differing from the originating tumor. Genomic events that were private to the PDOX correspond to classical glioma aberrations, known to be heterogeneous late events in GBM [54, 96], supporting the notion that the PDOX-dominating clones were a result of original intratumor heterogeneity revealed by sampling and natural glioma evolution over time. In contrast to a previous analysis of subcutaneous PDX [7], we did not detect any recurrent genetic changes across the cohort suggesting that the interaction of human tumor cells with mouse TME does not influence genetic features of the tumor per se. Minor changes in clonal trajectories have also been observed in certain PDX from GBMs [106], brain metastases [101] and other cancers [40, 46]. In this respect, PDOX models can be considered as a proxy for dynamic clonal evolution, which is difficult to measure in patients. We also did not observe major changes in paired longitudinal glioma samples neither in the parental patient tumor nor in the corresponding PDOX, in accordance with limited treatment-induced clonal evolution in diffuse gliomas [5]. We report a case of clonal evolution from *EGFRvII* to *EGFRvIII*, which was recapitulated in the corresponding PDOXs. Although *EGFRvIII* may be lost upon recurrence, cases with acquisition of this variant were also reported [38, 110]. Interestingly, longitudinal models also retained state-specific intratumoral heterogeneity and genetic subclones, highlighting the notion that these unique matched PDOXs provide an ideal platform to study specific molecular events in initial and recurrent disease side by side. We further show that propagation of GBM cells grown as GSCs *in vitro* leads to a faster genetic drift, including ploidy changes, and acquisition of new CNAs and genetic variants.

At scale tumor-intrinsic epigenetic and transcriptomic profiles of individual tumors were well recapitulated in PDOX. Our PDOX cohort represents diverse molecular subtypes and retains intratumoral heterogeneity and plasticity, in particular, we show that GBM PDOX display cellular state transitions recently described in patient samples [77]. No major molecular changes or selection of cellular subpopulations were detected, except for those related to the replacement of human TME by mouse counterparts. These changes are expected in bulk tissue analyses where methylation and transcriptome profiles are biased by TME-derived signals [56, 112]. In line with the previous reports [6, 88] *in vitro* cell lines showed increased global DNA methylation levels and more profound changes in transcriptomic profiles.

Limitations of PDOX models include possible interspecies differences at the molecular level and the lack of a complete immune system in immunocompromised animals. While the adaptive immune system is largely absent in these mice, they retain a largely functional innate immune system, including microglia, the brain resident immune effector cells, and peripheral myeloid cells. GBM are largely lymphocyte depleted tumors [102], while microglia and

macrophages constitute the major immune component [82]. Here we show that classical glioma TME components such as microglia/macrophages, astrocytes, and OPCs are present in xenografted tumors, indicating that tumor cell interactions with the TME remain active in PDOX. Of note, we observe a similar transcriptomic shift in tumor-associated microglia/macrophages as described in GBM patients [31, 113]. It remains to be determined to what extent these models will be amenable to immunotherapeutic studies targeting tumor-associated microglia/macrophages. Although challenging, adaptation of glioma PDOXs to a humanized background might be possible and/or studies in an immunocompetent context could be performed with PDOX-derived organoids co-cultured with autologous immune cells.

Other drawbacks of patient-derived (orthotopic) xenografts, include high costs, complex logistics and an inherent low-throughput nature. Large-scale *in vivo* screens are possible; however, they are laborious and require specific statistical settings [46]. Expansion of human gliomas in PDOX and initial drug screens performed on PDOX-derived organoids appears as a good compromise between retention of glioma hallmarks and a cost-effective drug testing pipeline. In contrast to patient-derived short-term cultures and organoids [51, 64], it allows for tumor expansion and *in vivo* validation. We have developed our protocols to reconstitute 3D organoids of equal size, which allow for reproducible drug testing. Downscaling of cell number per organoid facilitated drug delivery, viability detection, and upscaling to high-throughput screens. These protocols can also be adapted to reintroduce TME components [12] and immune cells. We show that PDOX-derived organoids show clinically relevant responses: (1) organoids with *MGMT* promoter methylation showed higher sensitivity to TMZ, (2) *CDK4/6* amplified organoids responded better to *CDK4/6* inhibitors, (3) organoids carrying *EGFR R108K*, *G598V*, and *A289T* gain-of-function mutations were most sensitive to Erlotinib and AZD3759, whereas EGFR low tumors were most resistant. Although *EGFRvIII* [73] and deletions in the C-terminal domain ( $\Delta 25-27/28$ ) were shown to sensitize GBM cells to Erlotinib [25], none of the EGFR structural variants present in our testing group systematically sensitized tumors to any of the EGFR inhibitors. Of note, the tested organoids displayed *P TEN* loss, a known resistance factor leading to dissociation of EGFR inhibition from downstream PI3K pathway inhibition [73]. Remarkably, VAL-083 showed a significantly better response than TMZ against GBMs of different genetic backgrounds and irrespective of *MGMT* status. VAL-083 was able to overcome TMZ resistance in recurrent GBM and its efficacy was confirmed *in vivo*, with no toxicity observed, lending optimism to ongoing clinical trials.

Overall, our glioma PDOX cohort provides a powerful platform for understanding tumor biology and preclinical treatment interventions at the individual patient level. So

far, the co-clinical use of glioma PDOXs as patient avatars for treatment prediction remains challenging as in most cases the time to establish PDOXs in sufficient quantity required for preclinical drug testing (generation 2–3) takes longer than the survival of most high-grade glioma patients. Instead, PDOXs can play a key role as a preclinical platform in ‘mouse clinical trials’ [114] for personalized medicine regimens. Organoid cultures are further an excellent tool for high-throughput drug intervention studies at lower cost and can be used directly either established from the patient tumor tissue or from PDOXs. Longitudinal models further constitute a robust tool for the analysis of tumor evolution and resistance mechanisms following targeted or untargeted treatments. By sharing the models and molecular data, we aim to facilitate large collaborative future preclinical trials.

**Acknowledgements** We are grateful to the Clinical and Epidemiological Investigation Center (CIEC) of the LIH for support in tumor collection, and to Jean-Jacques Gerardy and Nathalie Nicot for technical assistance. We thank the Helmholtz Zentrum München (Research Unit of Molecular Epidemiology/Institute of Epidemiology, German Research Center for Environmental Health, Neuherberg, Germany) for processing the EPIC DNA methylation arrays. We acknowledge the financial support by the Luxembourg Institute of Health, Télévie-FNRS (Grants TETHER n°7.4632.17 and n°7.4615.18), Fondation Cancer Luxembourg (Pan-RTK Targeting), the Luxembourg National Research Fund (FNR; CORE Junior C17/BM/11664971/DEMICS, AFR/14206478 TregBar, INTER/DFG/17/11583046 MechEPI) and the GLIOTRAIN ITN funded by the European Union’s Horizon 2020 research and innovation programme under the Marie Skłodowska-Curie grant agreement No 766069 (The material presented and views expressed here are the responsibility of the author(s) only. The EU Commission takes no responsibility for any use made of the information set out). MM would like to thank the Luxembourg National Research Fund (FNR) for the support (FNR PEARL P16/BM/11192868 grant).

**Author contribution** Conceptualization: AG, A-CH, AO, RB, SPN; methodology: AG, A-CH, AO, DS, AIS, SPN; investigation: AG, A-CH, AO, DS, YAY, ViB, VaB, EK, SB, OK, AIM, ADF, LR, SP, AIM, MM, formal analysis: AG, A-CH, AO, DS, YAY, VN, MW, ArM, TK, PVN, FA, ADF, BF, SP, TA, ArM, PM, HM, TMM, HN, Y-JK, WJ, BK, GT, LFS, resources: AIM, CH-M, AnS, DB, HM, AIS, FH, RB, SPN, supervision: AG, CH-M, BK, LFS, MM, AIS, RB, SPN, writing—original draft: AG, A-CH, SPN, writing—review & editing: all authors.

## Compliance with ethical standards

**Conflict of interest** D Brown is CSO at Delmar Pharmaceuticals, A. Steino was preclinical study manager at Delmar Pharmaceuticals. A Golebiewska and S.P. Niclou received a research grant from Delmar Pharmaceuticals. No potential conflict of interest was disclosed by other authors.

**Open Access** This article is licensed under a Creative Commons Attribution 4.0 International License, which permits use, sharing, adaptation, distribution and reproduction in any medium or format, as long as you give appropriate credit to the original author(s) and the source, provide a link to the Creative Commons licence, and indicate if changes were made. The images or other third party material in this article are

included in the article’s Creative Commons licence, unless indicated otherwise in a credit line to the material. If material is not included in the article’s Creative Commons licence and your intended use is not permitted by statutory regulation or exceeds the permitted use, you will need to obtain permission directly from the copyright holder. To view a copy of this licence, visit <http://creativecommons.org/licenses/by/4.0/>.

## References

1. Abdul Rahim SA, Dirkse A, Oudin A, Schuster A, Bohler J, Barthelmy V et al (2017) Regulation of hypoxia-induced autophagy in glioblastoma involves ATG9A. *Br J Cancer* 117:813–825. <https://doi.org/10.1038/bjc.2017.263>
2. Aldape K, Brindle KM, Chesler L, Chopra R, Gajjar A, Gilbert MR et al (2019) Challenges to curing primary brain tumours. *Nat Rev Clin Oncol* 16:509–520. <https://doi.org/10.1038/s41571-019-0177-5>
3. Alonso R, Salavert F, Garcia-Garcia F, Carbonell-Caballero J, Bleda M, Garcia-Alonso L et al (2015) Babelomics 5.0: functional interpretation for new generations of genomic data. *Nucleic Acids Res* 43:W117–121. <https://doi.org/10.1093/nar/gkv384>
4. Balvers RK, Kleijn A, Kloezeman JJ, French PJ, Kremer A, van den Bent MJ et al (2013) Serum-free culture success of glial tumors is related to specific molecular profiles and expression of extracellular matrix-associated gene modules. *Neuro Oncol* 15:1684–1695. <https://doi.org/10.1093/neuonc/not116>
5. Barthel FP, Johnson KC, Varn FS, Moskalik AD, Tanner G, Kocakavuk E et al (2019) Longitudinal molecular trajectories of diffuse glioma in adults. *Nature*. <https://doi.org/10.1038/s41586-019-1775-1>
6. Baskaran S, Mayrhofer M, Kultima HG, Bergstrom T, Elfineh L, Cavelier L et al (2018) Primary glioblastoma cells for precision medicine: a quantitative portrait of genomic (in)stability during the first 30 passages. *Neuro Oncol* 20:1080–1091. <https://doi.org/10.1093/neuonc/ny024>
7. Ben-David U, Ha G, Tseng YY, Greenwald NF, Oh C, Shih J et al (2017) Patient-derived xenografts undergo mouse-specific tumor evolution. *Nat Genet* 49:1567–1575. <https://doi.org/10.1038/ng.3967>
8. Benjamini Y, Hochberg Y (1995) Controlling the false discovery rate: a practical and powerful approach to multiple testing. *J R Stat Soc Ser B (Methodol)* 57:289–300
9. Binder ZA, Thorne AH, Bakas S, Wileyto EP, Billello M, Akbari H et al (2018) Epidermal growth factor receptor extracellular domain mutations in glioblastoma present opportunities for clinical imaging and therapeutic development. *Cancer Cell* 34(163–177):e167. <https://doi.org/10.1016/j.ccell.2018.06.006>
10. Bjerkvig R, Tonnesen A, Laerum OD, Backlund EO (1990) Multicellular tumor spheroids from human gliomas maintained in organ culture. *J Neurosurg* 72:463–475. <https://doi.org/10.3171/jns.1990.72.3.0463>
11. Bonavia R, Inda MM, Cavenee WK, Furnari FB (2011) Heterogeneity maintenance in glioblastoma: a social network. *Cancer Res* 71:4055–4060. <https://doi.org/10.1158/0008-5472.CAN-11-0153>
12. Bougnaud S, Golebiewska A, Oudin A, Keunen O, Harter PN, Mader L et al (2016) Molecular crosstalk between tumour and brain parenchyma instructs histopathological features in glioblastoma. *Oncotarget* 7:31955–31971. <https://doi.org/10.18632/oncotarget.7454>
13. Brabetz S, Leary SES, Grobner SN, Nakamoto MW, Seker-Cin H, Girard EJ et al (2018) A biobank of patient-derived

- pediatric brain tumor models. *Nat Med* 24:1752–1761. <https://doi.org/10.1038/s41591-018-0207-3>
14. Brennan CW, Verhaak RG, McKenna A, Campos B, Nounshmehr H, Salama SR et al (2013) The somatic genomic landscape of glioblastoma. *Cell* 155:462–477. <https://doi.org/10.1016/j.cell.2013.09.034>
  15. Butler A, Hoffman P, Smibert P, Papalexi E, Satija R (2018) Integrating single-cell transcriptomic data across different conditions, technologies, and species. *Nat Biotechnol* 36:411–420. <https://doi.org/10.1038/nbt.4096>
  16. Byrne AT, Alferez DG, Amant F, Annibaldi D, Arribas J, Biankin AV et al (2017) Interrogating open issues in cancer precision medicine with patient-derived xenografts. *Nat Rev Cancer* 17:254–268. <https://doi.org/10.1038/nrc.2016.140>
  17. Callari M, Batra AS, Batra RN, Sammut SJ, Greenwood W, Clifford H et al (2018) Computational approach to discriminate human and mouse sequences in patient-derived tumour xenografts. *BMC Genomics* 19:19. <https://doi.org/10.1186/s12864-017-4414-y>
  18. Campos B, Wan F, Farhadi M, Ernst A, Zeppernick F, Tagscherer KE et al (2010) Differentiation therapy exerts antitumor effects on stem-like glioma cells. *Clin Cancer Res* 16:2715–2728
  19. Cancer Genome Atlas Research N, Weinstein JN, Collisson EA, Mills GB, Shaw KR, Ozenberger BA et al (2013) The Cancer Genome Atlas Pan-Cancer analysis project. *Nat Genet* 45:1113–1120. <https://doi.org/10.1038/ng.2764>
  20. Capper D, Jones DTW, Sill M, Hovestadt V, Schrimpf D, Sturm D et al (2018) DNA methylation-based classification of central nervous system tumours. *Nature* 555:469–474. <https://doi.org/10.1038/nature26000>
  21. Carlson BL, Pokorny JL, Schroeder MA, Sarkaria JN (2011) Establishment, maintenance and in vitro and in vivo applications of primary human glioblastoma multiforme (GBM) xenograft models for translational biology studies and drug discovery. *Curr Protoc Pharmacol Chapter* 14:14–16. <https://doi.org/10.1002/0471141755.ph1416s52>
  22. Ceccarelli M, Barthel FP, Malta TM, Sabedot TS, Salama SR, Murray BA et al (2016) Molecular profiling reveals biologically discrete subsets and pathways of progression in diffuse glioma. *Cell* 164:550–563. <https://doi.org/10.1016/j.cell.2015.12.028>
  23. Chen S, Zhou Y, Chen Y, Gu J (2018) fastp: an ultra-fast all-in-one FASTQ preprocessor. *Bioinformatics* 34:i884–i890. <https://doi.org/10.1093/bioinformatics/bty560>
  24. Chen X, Schulz-Trieglaff O, Shaw R, Barnes B, Schlesinger F, Kallberg M et al (2016) Manta: rapid detection of structural variants and indels for germline and cancer sequencing applications. *Bioinformatics* 32:1220–1222. <https://doi.org/10.1093/bioinformatics/btv710>
  25. Cho J, Pastorino S, Zeng Q, Xu X, Johnson W, Vandenberg S et al (2011) Glioblastoma-derived epidermal growth factor receptor carboxyl-terminal deletion mutants are transforming and are sensitive to EGFR-directed therapies. *Cancer Res* 71:7587–7596. <https://doi.org/10.1158/0008-5472.CAN-11-0821>
  26. Christensen K, Aaberg-Jessen C, Andersen C, Goplen D, Bjerkvig R, Kristensen BW (2010) Immunohistochemical expression of stem cell, endothelial cell, and chemosensitivity markers in primary glioma spheroids cultured in serum-containing and serum-free medium. *Neurosurgery* 66:933–947. <https://doi.org/10.1227/01.NEU.0000368393.45935.46>
  27. Cingolani P, Platts A, Wang L, Coon M, Nguyen T, Wang L et al (2012) A program for annotating and predicting the effects of single nucleotide polymorphisms, SnpEff: SNPs in the genome of *Drosophila melanogaster* strain w1118; iso-2; iso-3. *Fly (Austin)* 6:80–92. <https://doi.org/10.4161/fly.19695>
  28. Claes A, Schuurinckx J, Boots-Sprenger S, Hendriks-Cornelissen S, Dekkers M, van der Kogel AJ et al (2008) Phenotypic and genotypic characterization of orthotopic human glioma models and its relevance for the study of anti-glioma therapy. *Brain Pathol* 18:423–433. <https://doi.org/10.1111/j.1750-3639.2008.00141.x>
  29. Consortium G (2018) Glioma through the looking GLASS: molecular evolution of diffuse gliomas and the Glioma Longitudinal Analysis Consortium. *Neuro Oncol* 20:873–884. <https://doi.org/10.1093/neuonc/nyo020>
  30. Conte N, Mason JC, Halmagyi C, Neuhauser S, Mosaku A, Yordanova G et al (2019) PDX Finder: a portal for patient-derived tumor xenograft model discovery. *Nucleic Acids Res* 47:D1073–D1079. <https://doi.org/10.1093/nar/gky984>
  31. Darmanis S, Sloan SA, Croote D, Mignardi M, Chernikova S, Samghabadi P et al (2017) Single-Cell RNA-seq analysis of infiltrating neoplastic cells at the migrating front of human glioblastoma. *Cell reports* 21:1399–1410. <https://doi.org/10.1016/j.celrep.2017.10.030>
  32. de Groot JF, Fuller G, Kumar AJ, Piao Y, Eterovic K, Ji Y et al (2010) Tumor invasion after treatment of glioblastoma with bevacizumab: radiographic and pathologic correlation in humans and mice. *Neuro Oncol* 12:233–242. <https://doi.org/10.1093/neuonc/nop027>
  33. de Souza CF, Sabedot TS, Malta TM, Stetson L, Morozova O, Sokolov A et al (2018) A distinct DNA methylation shift in a subset of glioma CpG island methylator phenotypes during tumor recurrence. *Cell reports* 23:637–651. <https://doi.org/10.1016/j.celrep.2018.03.107>
  34. De Witt Hamer PC, Van Tilborg AA, Eijk PP, Sminia P, Troost D, Van Noorden CJ et al (2008) The genomic profile of human malignant glioma is altered early in primary cell culture and preserved in spheroids. *Oncogene* 27:2091–2096
  35. deCarvalho AC, Kim H, Poisson LM, Winn ME, Mueller C, Cherba D, Koeman J, Seth S et al (2018) Discordant inheritance of chromosomal and extrachromosomal DNA elements contributes to dynamic disease evolution in glioblastoma. *Nat Genet* 50:708–717. <https://doi.org/10.1038/s41588-018-0105-0>
  36. Dirkse A, Golebiewska A, Buder T, Nazarov PV, Muller A, Poovathingal S et al (2019) Stem cell-associated heterogeneity in Glioblastoma results from intrinsic tumor plasticity shaped by the microenvironment. *Nature Commun* 10:1787. <https://doi.org/10.1038/s41467-019-09853-z>
  37. Doh I, Kwon YJ, Ku B, Lee DW (2019) Drug efficacy comparison of 3D forming and preforming sphere models with a micro-pillar and microwell chip platform. *SLAS Disc Adv Life Sci R & D* 24:476–483. <https://doi.org/10.1177/2472555218821292>
  38. Draaisma K, Chatzipli A, Taphoorn M, Kerkhof M, Weyerbrock A, Sanson M et al (2019) Molecular Evolution of IDH wild-type glioblastomas treated with standard of care affects survival and design of precision medicine trials: a report from the EORTC 1542 study. *J Clin Oncol*. <https://doi.org/10.1200/JCO.19.00367>
  39. Eckhardt S, Csetenyi J, Horvath IP, Kerpel-Fronius S, Szamel I, Institoris L et al (1977) Uptake of labeled dianhydrogalactitol into human gliomas and nervous tissue. *Cancer Treat Rep* 61:841–847
  40. Eirew P, Steif A, Khattra J, Ha G, Yap D, Farahani H et al (2015) Dynamics of genomic clones in breast cancer patient xenografts at single-cell resolution. *Nature* 518:422–426. <https://doi.org/10.1038/nature13952>
  41. Eskilsson E, Rosland GV, Solecki G, Wang Q, Harter PN, Graziani G et al (2018) EGFR heterogeneity and implications for therapeutic intervention in glioblastoma. *Neuro Oncol* 20:743–752. <https://doi.org/10.1093/neuonc/nox191>
  42. Evrard YA, Srivastava A, Randjelovic J, Consortium NP, Doroshov JH, Dean DA et al (2020) Systematic establishment of robustness and standards in patient-derived


- xenograft experiments and analysis. *Cancer Res.* <https://doi.org/10.1158/0008-5472.CAN-19-3101>
43. Fack F, Tardito S, Hochart G, Oudin A, Zheng L, Fritah S et al (2017) Altered metabolic landscape in IDH-mutant gliomas affects phospholipid, energy, and oxidative stress pathways. *EMBO Mol Med* 9:1681–1695. <https://doi.org/10.15252/emmm.201707729>
  44. Francies HE, Barthorpe A, McLaren-Douglas A, Barendt WJ, Garnett MJ (2019) Drug sensitivity assays of human cancer organoid cultures. *Methods Mol Biol* 1576:339–351. [https://doi.org/10.1007/7651\\_2016\\_10](https://doi.org/10.1007/7651_2016_10)
  45. Francis JM, Zhang CZ, Maire CL, Jung J, Manzo VE, Adalsteinsson VA et al (2014) EGFR variant heterogeneity in glioblastoma resolved through single-nucleus sequencing. *Cancer Discov* 4:956–971. <https://doi.org/10.1158/2159-8290.CD-13-0879>
  46. Gao H, Korn JM, Ferretti S, Monahan JE, Wang Y, Singh M et al (2015) High-throughput screening using patient-derived tumor xenografts to predict clinical trial drug response. *Nature Med* 21:1318–1325. <https://doi.org/10.1038/nm.3954>
  47. Golebiewska A, Bounaud S, Stieber D, Brons NH, Vallar L, Hertel F et al (2013) Side population in human glioblastoma is non-tumorigenic and characterizes brain endothelial cells. *Brain J Neurol* 136:1462–1475. <https://doi.org/10.1093/brain/awt025>
  48. Hegi ME, Diserens AC, Gorlia T, Hamou MF, de Tribolet N, Weller M et al (2005) MGMT gene silencing and benefit from temozolomide in glioblastoma. *N Engl J Med* 352:997–1003. <https://doi.org/10.1056/NEJMoa043331>
  49. Hubert CG, Rivera M, Spangler LC, Wu Q, Mack SC, Prager BC et al (2016) A three-dimensional organoid culture system derived from human glioblastomas recapitulates the hypoxic gradients and cancer stem cell heterogeneity of tumors found in vivo. *Cancer Res* 76:2465–2477. <https://doi.org/10.1158/0008-5472.CAN-15-2402>
  50. Hulten A, Kerstell J, Larsson J, Olsson R, Svanborg A (1968) A method of calculating the nursing work load. *Lakartidningen* 65:1683–1686
  51. Jacob F, Salinas RD, Zhang DY, Nguyen PTT, Schnoll JG, Wong SZH et al (2020) A Patient-Derived Glioblastoma Organoid Model And Biobank Recapitulates Inter- And Intra-Tumoral Heterogeneity. *Cell* 180(188–204):e122. <https://doi.org/10.1016/j.cell.2019.11.036>
  52. Joo KM, Kim J, Jin J, Kim M, Seol HJ, Muradov J et al (2013) Patient-specific orthotopic glioblastoma xenograft models recapitulate the histopathology and biology of human glioblastomas in situ. *Cell reports* 3:260–273. <https://doi.org/10.1016/j.celrep.2012.12.013>
  53. Keunen O, Johansson M, Oudin A, Sanzey M, Abdul Rahim SA, Fack F et al (2011) Anti-VEGF treatment reduces blood supply and increases tumor cell invasion in glioblastoma. *Proc Natl Acad Sci USA.* <https://doi.org/10.1073/pnas.1014480108>
  54. Kim H, Zheng S, Amini SS, Virk SM, Mikkelsen T, Brat DJ et al (2015) Whole-genome and multisector exome sequencing of primary and post-treatment glioblastoma reveals patterns of tumor evolution. *Genome Res* 25:316–327. <https://doi.org/10.1101/gr.180612.114>
  55. Klink B, Miletic H, Stieber D, Huszthy PC, Valenzuela JA, Bals J et al (2013) A novel, diffusely infiltrative xenograft model of human anaplastic oligodendroglioma with mutations in FUBP1, CIC, and IDH1. *PLoS One* 8:e59773. <https://doi.org/10.1371/journal.pone.0059773>
  56. Klughammer J, Kiesel B, Roetzer T, Fortelny N, Nemc A, Nennig KH et al (2018) The DNA methylation landscape of glioblastoma disease progression shows extensive heterogeneity in time and space. *Nat Med* 24:1611–1624. <https://doi.org/10.1038/s41591-018-0156-x>
  57. Korber V, Yang J, Barah P, Wu Y, Stichel D, Gu Z et al (2019) Evolutionary trajectories of IDH(WT) glioblastomas reveal a common path of early tumorigenesis instigated years ahead of initial diagnosis. *Cancer Cell* 35(692–704):e612. <https://doi.org/10.1016/j.ccell.2019.02.007>
  58. Koster J, Rahmann S (2018) Snakemake—a scalable bioinformatics workflow engine. *Bioinformatics* 34:3600. <https://doi.org/10.1093/bioinformatics/bty350>
  59. Kriebel J, Herder C, Rathmann W, Wahl S, Kunze S, Molnos S et al (2016) Association between DNA Methylation in whole blood and measures of glucose metabolism: KORA F4 study. *Plos One* 11:e0152314. <https://doi.org/10.1371/journal.pone.0152314>
  60. Kristensen BW, Priesterbach-Ackley LP, Petersen JK, Wesseling P (2019) Molecular pathology of tumors of the central nervous system. *Ann Oncol.* <https://doi.org/10.1093/annonc/mdz164>
  61. Landrum MJ, Lee JM, Benson M, Brown GR, Chao C, Chitipiralla S et al (2018) ClinVar: improving access to variant interpretations and supporting evidence. *Nucleic Acids Res* 46:D1062–D1067. <https://doi.org/10.1093/nar/gkx1153>
  62. Lee J, Kotliarova S, Kotliarov Y, Li A, Su Q, Domin NM et al (2006) Tumor stem cells derived from glioblastomas cultured in bFGF and EGF more closely mirror the phenotype and genotype of primary tumors than do serum-cultured cell lines. *Cancer Cell* 9:391–403. <https://doi.org/10.1016/j.ccr.2006.03.030>
  63. Lee JC, Vivanco I, Beroukhir M, Huang JH, Feng WL, DeBiasi RM et al (2006) Epidermal growth factor receptor activation in glioblastoma through novel missense mutations in the extracellular domain. *PLoS Med* 3:e485. <https://doi.org/10.1371/journal.pmed.0030485>
  64. Lee JK, Liu Z, Sa JK, Shin S, Wang J, Bordyuh M et al (2018) Pharmacogenomic landscape of patient-derived tumor cells informs precision oncology therapy. *Nat Genet* 50:1399–1411. <https://doi.org/10.1038/s41588-018-0209-6>
  65. Li H, Handsaker B, Wysoker A, Fennell T, Ruan J, Homer N et al (2009) The Sequence alignment/map format and SAMtools. *Bioinformatics* 25:2078–2079. <https://doi.org/10.1093/bioinformatics/btp352>
  66. Liffers K, Lamszus K, Schulte A (2015) EGFR amplification and glioblastoma stem-like cells. *Stem Cells Int* 2015:427518. <https://doi.org/10.1155/2015/427518>
  67. Louis DN, Perry A, Reifenberger G, von Deimling A, Figarella-Branger D, Cavenee WK et al (2016) The 2016 world health organization classification of tumors of the central nervous system: a summary. *Acta Neuropathol* 131:803–820. <https://doi.org/10.1007/s00401-016-1545-1>
  68. Luchman HA, Chesnelong C, Cairncross JG, Weiss S (2013) Spontaneous loss of heterozygosity leading to homozygous R132H in a patient-derived IDH1 mutant cell line. *Neuro Oncol* 15:979–980. <https://doi.org/10.1093/neuonc/not064>
  69. Luchman HA, Stechishin OD, Dang NH, Blough MD, Chesnelong C, Kelly JJ et al (2012) An in vivo patient-derived model of endogenous IDH1-mutant glioma. *Neuro Oncol* 14:184–191. <https://doi.org/10.1093/neuonc/nor207>
  70. Macosko EZ, Basu A, Satija R, Nemes J, Shekhar K, Goldman M et al (2015) Highly parallel genome-wide expression profiling of individual cells using nanoliter droplets. *Cell* 161:1202–1214. <https://doi.org/10.1016/j.cell.2015.05.002>
  71. Mahesparan R, Read TA, Lund-Johansen M, Skaftnesmo KO, Bjerkvig R, Engebraaten O (2003) Expression of extracellular matrix components in a highly infiltrative in vivo glioma model. *Acta Neuropathol* 105:49–57. <https://doi.org/10.1007/s00401-002-0610-0>
  72. Meehan TF, Conte N, Goldstein T, Inghirami G, Murakami MA, Brabetz S et al (2017) PDX-MI: minimal information for

- patient-derived tumor xenograft models. *Cancer Res* 77:e62–e66. <https://doi.org/10.1158/0008-5472.CAN-17-0582>
73. Mellingshoff IK, Wang MY, Vivanco I, Haas-Kogan DA, Zhu S, Dia EQ et al (2005) Molecular determinants of the response of glioblastomas to EGFR kinase inhibitors. *N Engl J Med* 353:2012–2024. <https://doi.org/10.1056/NEJMoa051918>
  74. Muller F, Scherer M, Assenov Y, Lutsik P, Walter J, Lengauer T et al (2019) RnBeads 2.0: comprehensive analysis of DNA methylation data. *Genome biology* 20:55. <https://doi.org/10.1186/s13059-019-1664-9>
  75. Navis AC, Niclou SP, Fack F, Stieber D, van Lith S, Verrijp K et al (2013) Increased mitochondrial activity in a novel IDH1-R132H mutant human oligodendroglioma xenograft model: in situ detection of 2-HG and alpha-KG. *Acta Neuropathol Commun* 1:18. <https://doi.org/10.1186/2051-5960-1-18>
  76. Nazarov PV, Wienecke-Baldacchino AK, Zinovyev A, Czerwinska U, Muller A, Nashan D et al (2019) Deconvolution of transcriptomes and miRNomes by independent component analysis provides insights into biological processes and clinical outcomes of melanoma patients. *BMC Med Genomics* 12:132. <https://doi.org/10.1186/s12920-019-0578-4>
  77. Neftel C, Laffy J, Filbin MG, Hara T, Shore ME, Rahme GJ et al (2019) An integrative model of cellular states, plasticity, and genetics for glioblastoma. *Cell* 178(835–849):e821. <https://doi.org/10.1016/j.cell.2019.06.024>
  78. Niclou SP, Danzeisen C, Eikesdal HP, Wiig H, Brons NH, Poli AM et al (2008) A novel eGFP-expressing immunodeficient mouse model to study tumor-host interactions. *Faseb J* 22:3120–3128. <https://doi.org/10.1096/fj.08-109611>
  79. Noshmeh H, Weisenberger DJ, Diefes K, Phillips HS, Pujara K, Berman BP et al (2010) Identification of a CpG island methylator phenotype that defines a distinct subgroup of glioma. *Cancer Cell* 17:510–522. <https://doi.org/10.1016/j.ccr.2010.03.017>
  80. Obad N, Espedal H, Jirik R, Sakariassen PO, Brekke Rygh C, Lund-Johansen M et al (2018) Lack of functional normalisation of tumour vessels following anti-angiogenic therapy in glioblastoma. *J Cerebral Blood Flow Metabol* 38:1741–1753. <https://doi.org/10.1177/0271678X17714656>
  81. Patel AP, Tirosh I, Trombetta JJ, Shalek AK, Gillespie SM, Wakimoto H et al (2014) Single-cell RNA-seq highlights intratumoral heterogeneity in primary glioblastoma. *Science* 344:1396–1401. <https://doi.org/10.1126/science.1254257>
  82. Pires-Afonso Y, Niclou SP, Michelucci A (2020) Revealing and harnessing tumour-associated microglia/macrophage heterogeneity in glioblastoma. *Int J Mol Sci*. <https://doi.org/10.3390/ijms21030689>
  83. Reis GF, Pekmezci M, Hansen HM, Rice T, Marshall RE, Molinaro AM et al (2015) CDKN2A loss is associated with shortened overall survival in lower-grade (World Health Organization Grades II-III) astrocytomas. *J Neuropathol Exp Neurol* 74:442–452. <https://doi.org/10.1097/NEN.0000000000000188>
  84. Roth A, Khattra J, Yap D, Wan A, Laks E, Biele J et al (2014) PyClone: statistical inference of clonal population structure in cancer. *Nat Methods* 11:396–398. <https://doi.org/10.1038/nmeth.2883>
  85. Sahn F, Schrimpf D, Jones DT, Meyer J, Kratz A, Reuss D et al (2016) Next-generation sequencing in routine brain tumor diagnostics enables an integrated diagnosis and identifies actionable targets. *Acta Neuropathol* 131:903–910. <https://doi.org/10.1007/s00401-015-1519-8>
  86. Sakariassen PO, Prestegarden L, Wang J, Skaftnesmo KO, Mahesparan R, Molthoff C et al (2006) Angiogenesis-independent tumor growth mediated by stem-like cancer cells. *Proc Natl Acad Sci USA* 103:16466–16471. <https://doi.org/10.1073/pnas.0607668103>
  87. Seshan VE, A O (2019) DNACopy: DNA copy number data analysis. R package version 1600
  88. Shen Y, Gridsdale CJ, Islam SA, Bose P, Lever J, Zhao EY et al (2019) Comprehensive genomic profiling of glioblastoma tumors, BTICs, and xenografts reveals stability and adaptation to growth environments. *Proc Natl Acad Sci USA* 116:19098–19108. <https://doi.org/10.1073/pnas.1813495116>
  89. Shirahata M, Ono T, Stichel D, Schrimpf D, Reuss DE, Sahn F et al (2018) Novel, improved grading system(s) for IDH-mutant astrocytic gliomas. *Acta Neuropathol* 136:153–166. <https://doi.org/10.1007/s00401-018-1849-4>
  90. Smyth G (2005) Limma: linear models for microarray data. In: Springer (ed) *Bioinformatics and Computational Biology Solutions using R and Bioconductor*. New York, pp 397–420
  91. Sottoriva A, Spiteri I, Piccirillo SG, Touloumis A, Collins VP, Marioni JC et al (2013) Intratumor heterogeneity in human glioblastoma reflects cancer evolutionary dynamics. *Proc Natl Acad Sci USA* 110:4009–4014. <https://doi.org/10.1073/pnas.1219747110>
  92. Stieber D, Golebiewska A, Evers L, Lenkiewicz E, Brons NH, Nicot N et al (2014) Glioblastomas are composed of genetically divergent clones with distinct tumorigenic potential and variable stem cell-associated phenotypes. *Acta Neuropathol* 127:203–219. <https://doi.org/10.1007/s00401-013-1196-4>
  93. Stuart T, Butler A, Hoffman P, Hafemeister C, Papalexi E, Mauck WM 3rd et al (2019) Comprehensive integration of single-cell data. *Cell* 177(1888–1902):e1821. <https://doi.org/10.1016/j.cell.2019.05.031>
  94. Stupp R, Mason WP, van den Bent MJ, Weller M, Fisher B, Taphoorn MJ et al (2005) Radiotherapy plus concomitant and adjuvant temozolomide for glioblastoma. *N Engl J Med* 352:987–996. <https://doi.org/10.1056/NEJMoa043330>
  95. Subramanian A, Tamayo P, Mootha VK, Mukherjee S, Ebert BL, Gillette MA et al (2005) Gene set enrichment analysis: a knowledge-based approach for interpreting genome-wide expression profiles. *Proc Natl Acad Sci USA* 102:15545–15550. <https://doi.org/10.1073/pnas.0506580102>
  96. Szerlip NJ, Pedraza A, Chakravarty D, Azim M, McGuire J, Fang Y et al (2012) Intratumoral heterogeneity of receptor tyrosine kinases EGFR and PDGFRA amplification in glioblastoma defines subpopulations with distinct growth factor response. *Proc Natl Acad Sci USA* 109:3041–3046. <https://doi.org/10.1073/pnas.1114033109>
  97. Talasila KM, Soentgerath A, Euskirchen P, Rosland GV, Wang J, Huszthy PC et al (2013) EGFR wild-type amplification and activation promote invasion and development of glioblastoma independent of angiogenesis. *Acta Neuropathol* 125:683–698. <https://doi.org/10.1007/s00401-013-1101-1>
  98. Talevich E, Shain AH, Botton T, Bastian BC (2016) CNVkit: Genome-Wide Copy Number Detection and Visualization from Targeted DNA Sequencing. *PLoS Comput Biol* 12:e1004873. <https://doi.org/10.1371/journal.pcbi.1004873>
  99. Tateishi K, Nakamura T, Juratli TA, Williams EA, Matsushita Y, Miyake S et al (2019) PI3K/AKT/mTOR pathway alterations promote malignant progression and xenograft formation in oligodendroglial tumors. *Clin Cancer Res* 25:4375–4387. <https://doi.org/10.1158/1078-0432.CCR-18-4144>
  100. Teschendorff AE, Marabita F, Lechner M, Bartlett T, Tegner J, Gomez-Cabrero D et al (2013) A beta-mixture quantile normalization method for correcting probe design bias in Illumina Infinium 450 k DNA methylation data. *Bioinformatics* 29:189–196. <https://doi.org/10.1093/bioinformatics/bts680>
  101. Tew BY, Legendre C, Schroeder MA, Triche T, Gooden GC, Huang Y et al (2019) Patient-derived xenografts of central nervous system metastasis reveal expansion of aggressive minor clones. *Neuro Oncol*. <https://doi.org/10.1093/neuonc/noz137>

102. Thorsson V, Gibbs DL, Brown SD, Wolf D, Bortone DS, Ou Yang TH et al (2018) The immune landscape of cancer. *Immunity* 48:812–830 e814. <https://doi.org/10.1016/j.immuni.2018.03.023>
103. Torsvik A, Stieber D, Enger PO, Golebiewska A, Molven A, Svendsen A et al (2014) U-251 revisited: genetic drift and phenotypic consequences of long-term cultures of glioblastoma cells. *Cancer Med* 3:812–824. <https://doi.org/10.1002/cam4.219>
104. Unruh D, Mirkov S, Wray B, Drumm M, Lamano J, Li YD et al (2019) Methylation-dependent tissue factor suppression contributes to the reduced malignancy of IDH1-mutant gliomas. *Clin Cancer Res* 25:747–759. <https://doi.org/10.1158/1078-0432.CCR-18-1222>
105. Van der Auwera GA, Carneiro MO, Hartl C, Poplin R, Del Angel G, Levy-Moonshine A et al (2013) From FastQ data to high confidence variant calls: the Genome Analysis Toolkit best practices pipeline. *Curr Protocols Bioinformatics* 43:111011–111033. <https://doi.org/10.1002/0471250953.bi1110s43>
106. Vaubel RA, Tian S, Remonde D, Schroeder MA, Mladek AC, Kitange GJ et al (2020) Genomic and phenotypic characterization of a broad panel of patient-derived xenografts reflects the diversity of glioblastoma. *Clin Cancer Res* 26:1094–1104. <https://doi.org/10.1158/1078-0432.CCR-19-0909>
107. Verhaak RG, Hoadley KA, Purdom E, Wang V, Qi Y, Wilkerson MD et al (2010) Integrated genomic analysis identifies clinically relevant subtypes of glioblastoma characterized by abnormalities in PDGFRA, IDH1, EGFR, and NF1. *Cancer CELL* 17:98–110. <https://doi.org/10.1016/j.ccr.2009.12.020>
108. Wakimoto H, Mohapatra G, Kanai R, Curry WT Jr, Yip S, Nitta M et al (2012) Maintenance of primary tumor phenotype and genotype in glioblastoma stem cells. *Neuro Oncol* 14:132–144. <https://doi.org/10.1093/neuonc/nor195>
109. Wakimoto H, Tanaka S, Curry WT, Loebel F, Zhao D, Tateishi K et al (2014) Targetable signaling pathway mutations are associated with malignant phenotype in IDH-mutant gliomas. *Clin Cancer Res* 20:2898–2909. <https://doi.org/10.1158/1078-0432.CCR-13-3052>
110. Wang J, Cazzato E, Ladewig E, Frattini V, Rosenbloom DI, Zairis S et al (2016) Clonal evolution of glioblastoma under therapy. *Nat Genet* 48:768–776. <https://doi.org/10.1038/ng.3590>
111. Wang J, Miletic H, Sakariassen PO, Huszthy PC, Jacobsen H, Brekka N et al (2009) A reproducible brain tumour model established from human glioblastoma biopsies. *BMC Cancer* 9:465. <https://doi.org/10.1186/1471-2407-9-465>
112. Wang Q, Hu B, Hu X, Kim H, Squatrito M, Scarpace L et al (2017) Tumor evolution of glioma-intrinsic gene expression subtypes associates with immunological changes in the microenvironment. *Cancer Cell* 32(42–56):e46. <https://doi.org/10.1016/j.ccell.2017.06.003>
113. Weng Q, Wang J, Wang J, He D, Cheng Z, Zhang F et al (2019) Single-cell transcriptomics uncovers glial progenitor diversity and cell fate determinants during development and gliomagenesis. *Cell Stem Cell* 24(707–723):e708. <https://doi.org/10.1016/j.stem.2019.03.006>
114. Williams JA (2018) Using PDX for preclinical cancer drug discovery: the evolving field. *J Clin Med*. <https://doi.org/10.3390/jcm7030041>
115. Woo XY, Giordano J, Srivastava A, Zhao Z-M, Lloyd MW, de Bruijn R et al (2019) Conservation of copy number profiles during engraftment and passing of patient-derived cancer xenografts. *bioRxiv:861393*. <https://doi.org/10.1101/861393>
116. Yang RR, Shi ZF, Zhang ZY, Chan AK, Aibaidula A, Wang WW et al (2019) IDH-mutant lower-grade (WHO Grades II/III) astrocytomas can be stratified for risk by CDKN2A, CDK4 and PDGFRA copy number alterations. *Brain Pathol*. <https://doi.org/10.1111/bpa.12801>
117. Zhai B, Steino A, Bacha J, Brown D, Daugaard M (2018) Dianhydrogalactitol induces replication-dependent DNA damage in tumor cells preferentially resolved by homologous recombination. *Cell Death Dis* 9:1016. <https://doi.org/10.1038/s41419-018-1069-9>
118. Zhou Y, Zhou B, Pache L, Chang M, Khodabakhshi AH, Tanaseichuk O et al (2019) Metascape provides a biologist-oriented resource for the analysis of systems-level datasets. *Nature Commun* 10:1523. <https://doi.org/10.1038/s41467-019-09234-6>

**Publisher's Note** Springer Nature remains neutral with regard to jurisdictional claims in published maps and institutional affiliations.

## Affiliations

Anna Golebiewska<sup>1</sup> · Ann-Christin Hau<sup>1</sup> · Anaïs Oudin<sup>1</sup> · Daniel Stieber<sup>1,2</sup> · Yahaya A. Yabo<sup>1,3</sup> · Virginie Baus<sup>1</sup> · Vanessa Barthelemy<sup>1</sup> · Eliane Klein<sup>1</sup> · Sébastien Bougnaud<sup>1</sup> · Olivier Keunen<sup>1,4</sup> · May Wantz<sup>1</sup> · Alessandro Michelucci<sup>1,5,6</sup> · Virginie Neirinckx<sup>1</sup> · Arnaud Muller<sup>4</sup> · Tony Kaoma<sup>4</sup> · Petr V. Nazarov<sup>4</sup> · Francisco Azuaje<sup>4</sup> · Alfonso De Falco<sup>2,3,7</sup> · Ben Flies<sup>2</sup> · Lorraine Richart<sup>3,7,8,9</sup> · Suresh Poovathingal<sup>6</sup> · Thais Arns<sup>6</sup> · Kamil Grzyb<sup>6</sup> · Andreas Mock<sup>10,11,12,13</sup> · Christel Herold-Mende<sup>10</sup> · Anne Steino<sup>14,15</sup> · Dennis Brown<sup>14,15</sup> · Patrick May<sup>6</sup> · Hrvoje Miletic<sup>16,17</sup> · Tathiane M. Malta<sup>18</sup> · Houtan Noushmehr<sup>18</sup> · Yong-Jun Kwon<sup>9</sup> · Winnie Jahn<sup>19,20</sup> · Barbara Klink<sup>2,9,19,20,21</sup> · Georgette Tanner<sup>22</sup> · Lucy F. Stead<sup>22</sup> · Michel Mittelbronn<sup>6,7,8,9</sup> · Alexander Skupin<sup>6</sup> · Frank Hertel<sup>6,23</sup> · Rolf Bjerkvig<sup>1,16</sup> · Simone P. Niclou<sup>1,16</sup> 

<sup>1</sup> NORLUX Neuro-Oncology Laboratory, Department of Oncology, Luxembourg Institute of Health, 84, Val Fleuri, 1526 Luxembourg, Luxembourg

<sup>2</sup> National Center of Genetics, Laboratoire National de Santé, 3555 Dudelange, Luxembourg

<sup>3</sup> Faculty of Science, Technology and Medicine, University of Luxembourg, 4367 Belvaux, Luxembourg

<sup>4</sup> Quantitative Biology Unit, Luxembourg Institute of Health, 1445 Strassen, Luxembourg

<sup>5</sup> Neuro-Immunology Group, Department of Oncology, Luxembourg Institute of Health, 1526 Luxembourg, Luxembourg

<sup>6</sup> Luxembourg Centre for Systems Biomedicine, University of Luxembourg, 4367 Belvaux, Luxembourg

- <sup>7</sup> Luxembourg Center of Neuropathology, Luxembourg, Luxembourg
- <sup>8</sup> National Center of Pathology, Laboratoire National de Santé, 3555 Dudelange, Luxembourg
- <sup>9</sup> Department of Oncology, Luxembourg Institute of Health, 1526 Luxembourg, Luxembourg
- <sup>10</sup> Division of Experimental Neurosurgery, Department of Neurosurgery, University of Heidelberg, 69120 Heidelberg, Germany
- <sup>11</sup> Department of Medical Oncology, National Center for Tumor Diseases (NCT) Heidelberg, Heidelberg University Hospital, 69120 Heidelberg, Germany
- <sup>12</sup> German Cancer Research Center (DKFZ) Heidelberg, 69120 Heidelberg, Germany
- <sup>13</sup> German Cancer Consortium (DKTK), 69120 Heidelberg, Germany
- <sup>14</sup> DelMar Pharmaceuticals, Inc., Vancouver, BC, Canada
- <sup>15</sup> DelMar Pharmaceuticals, Inc., Menlo Park, CA, USA
- <sup>16</sup> Department of Biomedicine, University of Bergen, 5019 Bergen, Norway
- <sup>17</sup> Department of Pathology, Haukeland University Hospital, Bergen, Norway
- <sup>18</sup> Department of Neurosurgery, Henry Ford Health System, Detroit, MI 48202, USA
- <sup>19</sup> German Cancer Consortium (DKTK), 01307 Dresden, Germany
- <sup>20</sup> Core Unit for Molecular Tumor Diagnostics (CMTD), National Center for Tumor Diseases (NCT), 01307 Dresden, Germany
- <sup>21</sup> Institute for Clinical Genetics, Faculty of Medicine Carl Gustav Carus, Technische Universität Dresden, Fetscherstraße 74, 01307 Dresden, Germany
- <sup>22</sup> Leeds Institute of Medical Research at St James's, St James's University Hospital, Leeds, UK
- <sup>23</sup> Department of Neurosurgery, Centre Hospitalier Luxembourg, 1210 Luxembourg, Luxembourg